Bulletin of the Mineral Research and Exploration

http://bulletin.mta.gov.tr

Coal quality, mineralogy, petrography, and geochemistry of the high-strontium Bozburun lignite (Malatya, eastern Türkiye)

Rıza Görkem OSKAY[a*]   and Ali İhsan KARAYİĞİT[b]

[a] Hacettepe University, Başkent OSB Technical Sciences Vocational School, Ankara, Türkiye

[b] Hacettepe University, Faculty of Engineering, Department of Geological Engineering, Ankara, Türkiye

Research Article

ABSTRACT

The Bozburun coalfield hosts a late Miocene 1.1 m thick coal seam. This study aims to determine coal quality, mineralogy, petrography and geochemistry, and controlling factors of elemental enrichments. The coals are generally black and greyish black in colour, and the low part of the seam commonly includes fossil shell remains. The ash yield displays a decreasing trend towards the upper part of the seam; in turn, gross calorific and total C values increase upwards. The total S content being generally higher than 5% (on dry basis), displays an increasing trend towards the upper part. In the entire seam, huminite is the most common maceral group, while inertinite and liptinite display variable proportions. The identified minerals by XRD are mainly quartz, clay minerals, calcite, pyrite, and aragonite (in fossil shell remains-bearing samples), whereas feldspars and marcasite determined in a few samples. Furthermore, in the coal samples, celestine and barite were identified by SEM-EDX. This study indicates that precipitation of celestine and Sr-bearing barite grains during diagenetic stage and Sr-uptake by mollusc within the palaeomire caused Sr enrichment in the entire seam. Overall, the water influx and redox conditions controlled the mineralogical and the elemental compositions of the coal seam.

1. Introduction

The mineralogical and geochemical features of coal and coal combustion remains have been the subject of several studies because of the hazardous elements and critical elements contained (e.g., Dai et al., 2012*a*, 2020*a*, *b*, 2021; Dai and Finkelman, 2018; Hower et al., 2020, 2022). Besides, more recent studies show that these features of coal beds and partings in combination with coal petrography, palaeontological, and sedimentological data could provide significant information about the depositional conditions in the palaeomires (e.g., Finkelman et al., 2019; Dai et al., 2020*a*; Hood et al., 2020) for this purpose, indicative elements, and element ratios have been used (e.g., Goodarzi and Swaine, 1994; Dai et al., 2015*a*, 2018, 2020*a*; Spiro et al., 2019). For example, distributions of As, U, and Mo contents, along with Th/U ratio, are used for the determination of palaeoredox conditions in palaeomires, while distributions of total S, B, and Mo contents and Sr/Ba ratio serves as palaeosalinity indicator in palaeomires (Goodarzi and Swaine, 1994; Spiro et al., 2019; Dai et al., 2020*a*; Goodarzi et al., 2020; Çelik et al., 2021). Nevertheless, these index elements and elemental ratios should be used with caution, since coal seams have heterogeneous elemental and mineralogical compositions and certain

accessory minerals (e.g., barite, chromite, monazite) can increase the concentrations of certain indicator elements (Finkelman et al., 2019; Dai et al., 2020a, b; Karayiğit et al., 2020a, b).

The petrographical and geochemical features of Turkish low-rank coals, particularly of the early-middle Miocene coals in western and central Anatolia, are well documented as a result of their use as feed coals in power plants (Querol et al., 1997; Karayiğit et al., 2000, 2017a; Tuncalı et al., 2002; Palmer et al., 2004). However, the coalfields of eastern Anatolia, with the exception of Kangal and Afşin-Elbistan coalfields, have received less attention (Karayiğit and Gayer, 2000; Karayiğit et al., 2001, 2019; Sütçü and Karayiğit, 2015). The tectonic evolution of eastern Anatolia during late Cenozoic times resulted in the formation of several sedimentary basins (e.g., Afşin-Elbistan, Gölbaşı, Sivas-Kangal and Malatya), which host mineable late Miocene and Plio-Pleistocene coal seams (Tuncalı et al., 2002; Kaymakçı et al., 2006; Sütçü and Karayiğit, 2015; Karayiğit et al., 2016; Yılmaz, 2019; Seyitoğlu et al., 2022). Another result of the tectonic activity is the development of regional volcanic activity from the early Miocene to Pliocene (Figure 1a) (Kocaaslan and Ersoy, 2018; Di Giuseppe

et al., 2021). Hence, volcanic complexes (Yamadağ and Kepezdağ) and volcanic fields (Kangal and Sivas) were developed.

The Bozburun coalfield is located in the Malatya Basin (Figure 2) and hosts a 1.1 m thick economic coal seam. Previous studies have mostly focused on the sedimentological and palaeontological properties of the Cenozoic sedimentary rocks and the petrogenesis of Cenozoic volcanic rocks in the Malatya Basin (Ercan and Asutay, 1993; Türkmen et al., 2004, 2007, 2011; Ekici et al., 2007; Nazik et al., 2008; Koç-Taşgın, 2011). Although coal seam exploitation in the study area began in early 1990s (Önal, 1995), only one coal geology study from the western part of the Bozburun coalfield has been conducted to date. In there, the coal seam displays relatively small thickness, and coal beds-bearing outcrops are located in the northern part of the Malatya Basin (Yalçın-Erik and Ay, 2020). The results of the previous coal geology study show that the coal displays significantly high ash yield and total sulphur content, and the coal is of subbituminous rank. The biomarker data supports the previous palynological results from Önal (1995) and Türkmen et al. (2004), indicating that the peat-forming vegetation was a mix of herbaceous
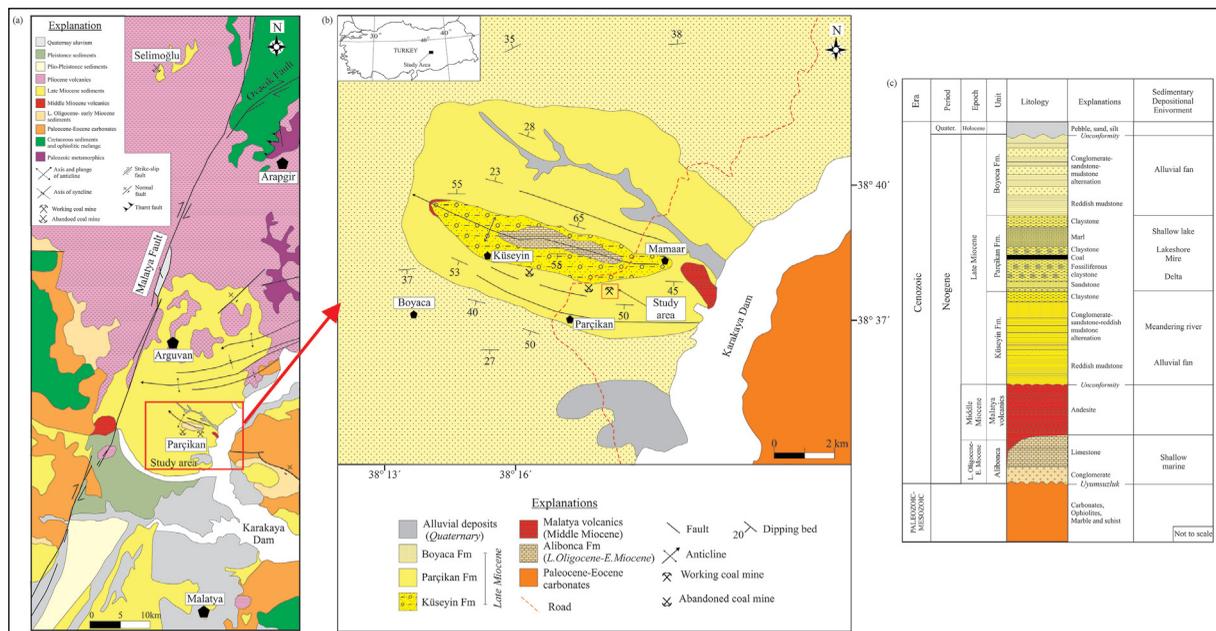
Figure 1- a) Regional geological map of the surrounding area of the Bozburun coalfield (modified from geological map of Türkiye, 1/500.000-scale), b) simplified geological map of the study area (modified from Türkmen et al., 2004; Sümengen, 2016), c) generalized stratigraphic column in the study area (modified from Türkmen et al., 2004).
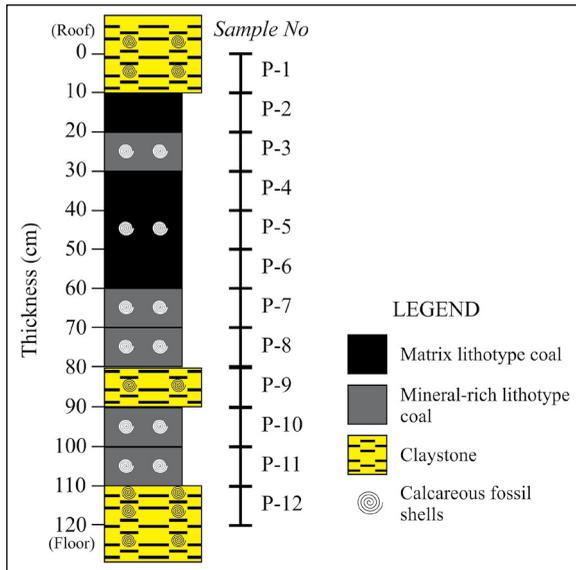
Figure 2- The sampled profile at the Bozburun coalfield.

and woody plants. Nevertheless, detailed elemental composition and paleoenvironmental reconstruction of the Bozburun coalfield are still lacking. Considering the volcanic activity in the Malatya Basin, the coal rank of the Bozburun coalfield might have differences from the northernmost of the Malatya Basin (Figure 1a). Therefore, this study focuses on determining the factors controlling the coal quality, the petrographical, mineralogical, and geochemical features of the late Miocene coal in the eastern part of the Bozburun coalfield and reconstructing the palaeoenvironment during the peat accumulation. The specific goal of the current study is to ascertain factors controlling coal rank variation in the Malatya Basin.

2. Geological Setting

The Bozburun coalfield is located in the southernmost of the NE–SW trending Malatya Basin, which is controlled by the Malatya Fault Zone (Figure 1a) (Kaymakçı et al., 2006; Sançar et al., 2019). The pre-Neogene basement consists of Permo-Triassic Keban metamorphics (marble and schist), middle Triassic-early Cretaceous Kuluncak ophiolite, late Cretaceous Elazığ magmatics (andesite, basalt, diorite, and gabbro), and Palaeocene to late Eocene marine carbonates with gypsum lenses and beds (Figure 1b-c) (Türkmen et al., 2007; Koç-Taşgın, 2011; Sümengen, 2016). The Malatya Basin begun developing during early Miocene due to regional extensional tectonic

regime (Kaymakçı et al., 2006). Thus, the Neogene basinal infillings started with late Oligocene (?)-early Miocene shallow marine deposits (Alibonca Formation), and this unit is conformably overlain by middle Miocene Malatya volcanics (andesite and basalt) of the Yamadağ volcanic complex (Ercan and Asutay, 1993; Önal, 1995; Türkmen et al., 2004, 2007; Koç-Taşgın, 2011; Sümengen, 2016; Kocaarslan and Ersoy, 2018; Di Giuseppe et al., 2021). Terrestrial conditions became dominant in the Malatya Basin during the late Miocene and these units inequitably overlay early-middle Miocene units (Figure 1c). The total thickness of late Miocene basinal infillings in the study area is around 1200 m and is divided into three formations (Türkmen et al., 2004, 2007; Nazik et al., 2008; Koç-Taşgın, 2011), from bottom to top, Küseyin Formation, Bozburun Formation, and Boyaca Formation (Figure 1c).

The Küseyin Formation is composed of alteration of conglomerate, sandstone, and reddish mudstone with freshwater mollusc-bearing limestone (Türkmen et al., 2004, 2007; Nazik et al., 2008; Koç-Taşgın, 2011). The sedimentological features of Küseyin Formation imply that the formation was deposited under alluvial fan and meandering river conditions where small freshwater ponds and lakes were developed (Türkmen et al., 2004, 2007; Koç-Taşgın, 2011). The ostracod fauna hosted in sediments suggest freshwater to oligohaline conditions (Nazik et al., 2008). The coal-bearing Bozburun Formation overlies conformably the Küseyin Formation and commences with current- or wave-ripple cross-laminatted sandstone, plant remains-bearing greyish green claystone, a coal seam, fossiliferous marl and limestone, and reddish mudstone (Türkmen et al., 2004, 2007; Sümengen, 2016) (Figure 1b). Previous sedimentological and palaeontological studies show that the Bozburun Formation was deposited in shallow lakes associated with peatlands and deltaic areas (Önal, 1995; Türkmen et al., 2004, 2007; Nazik et al., 2008). Furthermore, the identified palynoflora from the Bozburun coal seam implies that palaeomires were developed under freshwater lakeshore and floodplain conditions, while the ostracod and gastropod fauna from the Bozburun Formation show that freshwater and brackish conditions were developed during the late Miocene.

The Boyaca Formation is widely exposed in the study area and consists of reddish mudstone, mudstone, and an alternation of planar parallel-stratified conglomerate, planar cross-stratified sandstone, and reddish mudstone (Figure 1b), related to alluvial fan conditions (Türkmen et al., 2007; Koç-Taşgın, 2011). During late Miocene to Pliocene, a compressional tectonic regime caused the deformation of Miocene formations in the Malatya Basin, which could be observed as hydroplastic deformation horizons within the late Miocene formations (Kaymakçı et al., 2006; Koç-Taşgın, 2011) (Figure 1b). Even though late Pliocene basalt lava flows are common in the northern part of the Malatya Basin (Ercan and Asutay, 1993; Ekici et al., 2007; Kocaaslan and Ersoy, 2018; Di Giuseppe et al., 2021) Late Pliocene basalt lavas or volcanic rocks are not exposed within the Bozburun coalfield. Finally, all Neogene units are overlain by unconformably unconsolidated Quaternary sediments (pebbles, sand, and silt) (Figure 1c).

3. Samples and Applied Methodology

In this study, a total of twelve samples (nine coal, one floor, one roof, and one parting) were obtained from the working coal face of an underground mine in the eastern part of Bozburun coalfield (Figure 2). The lithotype descriptions of the coal samples were performed following the International Committee for Coal and Organic (ICCP) nomenclature (ICCP, 1993). Standard proximate, ultimate and petrographic analyses, as well as calorific determination were conducted at Hacetepe University. Coal petrography analyses were performed using polished blocks prepared according to the ASTM D2797/D2797M (2019) and examined under a coal petrography microscope. The maceral nomenclature followed ICCP System 1994 (ICCP, 2001; Sýkorová et al., 2005; Pickel et al., 2017). For rank determination, the mean random huminite reflectance measurements (%Rr) were exclusively performed on uliminite B following ISO 7404-5 (2009) standard.

For X-ray powder diffraction (XRD) analysis of raw coal and non-coal samples, a Bruker D8 equipment at the General Directorate of Mineral Research and Exploration (MTA) (Ankara, Türkiye) was used. EVA$^\rightarrow$ software (Bruker) was used for semi-

quantitative determination of the mineralogical composition of the samples. For a better detailed mineralogical composition and determining accessory phases selected six coal (P-4, -5, -6, -8, -10, -11) and two non-coal samples (P-1 and -9) examined using FEI Quanta 400 FEI-SEM-EDX at the MTA. For these examination polished blocs were coated with carbon. The powered raw coal and non-coal samples pellets with KBr mixture were examined using a Perkin Elmer Spectrum-II (Fourier transform-infrared spectrometry (FT-IR) instrument. The XRF, ICP-OES, and ICP–MS analyses of all samples were conducted at the MTA. The major oxide contents were determined from raw samples using XRF equipment. For determination of minor and trace elemental compositions using ICP-OES and MS analyses, all samples were firstly ashed at 550 °C, for complete the removing of organic fraction of samples, in a muffle furnace. The digested solutions were prepared from ashed samples using in perchloric acid, aqua regia, nitric acid and concentrated hydrochloric acid following Nadkarni (1980) methodology. Minor and trace elemental compositions were determined using ICP-OES and ICP-MS equipment. External and internal standards were used for checking the accuracy of the analyses.

4. Findings

4.1. Coal Quality

The coal samples are generally black and greyish black in colour. In the low part of the seam, calcareous fossil remains-bearing bands were identified. In the upper part of the seam, the matrix lithotype dominates, i.e., black-coloured gelified humic mass without any mineral impurities and/or with mineral impurities thinner than 1 mm, were identified. In the low part the mineral-rich lithotype prevails, i.e., greyish in colour and containing fossil shell remains-bearing thicker than 1 mm (Table 1, Figure 2). The roof rock sample is fossiliferous claystone, while the parting and floor rock samples are fossiliferous carbonaceous claystone (Figure 2). Furthermore, parting and roof rock samples also contain disseminated carbonized fossil plant litter remains.

Table 1- The results of proximate and ultimate analyses of coal and coal samples, as well as of the calorific value determination of coal samples ((VM: volatile matter, GCV: gross calorific value; asr: as-received basis; d: dry basis; daf: dry, ash-free basis; *oxygen content is calculated by subtraction [O = 100 − (C + H + S + N + ash)] on dry basis).

Sample No	Sampling Interval (cm)		Lithology for Non-coal samples/ Coal Lithotype	Moisture (wt.%, asr)	Ash yield	VM	GCV (MJ/kg, daf)	C	H	N	S	O*
					(wt.%, d)			(wt.%, d)				
P-1	0	10	Claystone	14.5	69.0	31.0	na	9.6	na	na	0.01	na
P-2	10	20	Matrix	25.6	30.6	40.9	28.4	49.9	5.4	1.2	6.8	6.1
P-3	20	30	Mineral-rich	24.4	48.3	35.0	26.2	36.5	4.3	0.8	6.3	3.8
P-4	30	40	Matrix	26.7	32.3	42.2	28.3	49.6	5.5	1.1	6.6	4.8
P-5	40	50	Matrix	22.3	32.0	43.4	28.5	50.5	5.4	1.1	6.4	4.5
P-6	50	60	Matrix	26.8	20.8	42.7	28.8	58.7	6.2	1.3	4.6	8.4
P-7	60	70	Mineral-rich	23.2	74.4	19.8	16.7	15.6	3.0	0.3	2.6	4.2
P-8	70	80	Mineral-rich	25.8	42.6	34.9	27.0	40.6	4.3	0.9	6.6	5.0
P-9	80	90	Carbonaceous claystone	17.1	62.0	38.0	na	12.8	na	na	0.1	na
P-10	90	100	Mineral-rich	19.6	60.6	39.4	8.6	17.4	1.5	0.1	0.3	20.1
P-11	100	110	Mineral-rich	19.4	62.7	37.3	6.7	15.6	1.4	0.1	0.4	19.8
P-12	110	120	Carbonaceous claystone	20.4	87.6	12.4	na	4.7	1.7	0.0	1.7	4.3

The ash yield displays a decreasing trend towards the upper part of the seam (Figure 3); in turn, the gross calorific value (GCV) and total C content are relatively high in this part. These trends are clearly related to the matrix lithotype in the upper part of the seam (Table 1). Furthermore, the total S content displays an increasing trend towards the upper part, where total S content is high (> 5%, on dry basis) (Table 1 and Figure 3). As expected, the volatile matter contents of fossil shell remain-bearing samples are deceptively higher than this in the other samples. This could be related to the breakdown of the calcareous remains (Table 1). Similarly, relatively high volatile matter content is also generally reported from fossil shell-bearing Turkish Cenozoic coalfields such as Afşin-Elbistan, Soma, Kangal, Milas, and Karapınar coalfields (Karayiğit et al., 2001, 2017a, 2019; Büçkün et al., 2015; Oskay et al., 2016, 2019). The hydrogen content of the matrix samples is relatively higher (5.4-6.2%, on dry basis) than this of the mineral-rich ones (1.4-4.3%, on dry basis).
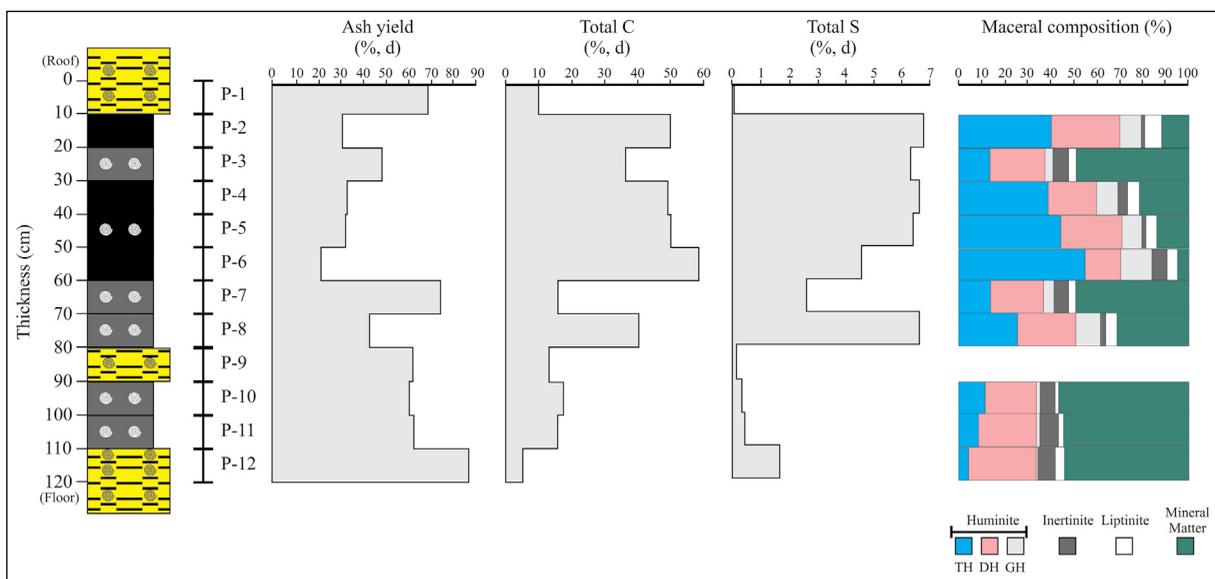
Figure 3- Vertical distribution of ash yield, total C and S, and maceral contents (on whole-basis) through the studied seam (for lithostratigraphic column, see Figure 2).

4.2. Maceral Composition and Huminite Reflectance

Huminite is the most common maceral group (34.1-84.5%, on a whole basis) in the studied samples, while inertinite (1.3-8.3%, on a whole-basis) and liptinite (1.5-6.7%, on a whole-basis) display variable proportions in the entire seam (Table 2 and Figure 3).

Telohuminite is the prevalent huminite maceral subgroup in the matrix lithotype samples, whereas detrohuminite displays generally higher proportions in the mineral-rich matrix samples (Figure 4). Textinite prevails generally in the matrix lithotype (Figures 4a-b) with telohuminite being mainly represented by ulminite (Figures 4a-c and e, and 5a). Porigelinite, resinite and corpohuminite commonly fill cell lumens of textinite (Figures 5a-b). The ulminite B variety is generally well gelified; however, the ulminite A variety exhibits very weak brownish fluorescence (Figures 5a-b). Densinite has higher proportions in the matrix samples, whereas in the mineral-rich ones, attrinite is more common. Inertinite (e.g., inertodetrinite and fusinite) and liptinite macerals (e.g., sporinite and liptodetrinite) are generally embedded within densinite (Figures 4d and 5c-d). Furthermore, attrinite appears generally within clay mineral aggregates (Figures 5c and f). Corpohuminite is the prevalent gelohuminite maceral in the coal samples and, as mentioned above, is mostly observed as cell-lumens infilling, as well as phlobaphinite (Figure 4a). The latter one could also be

an indicator of woody peat-forming plants (Sýkorová et al., 2005). As noted above, porigelinite is identified within telohuminite macerals (Figure 4b), while levigelinite is identified in the entire seam (Figure 4d).

The inertinite content is generally higher than 10% (on a mineral matter-free basis) in the low part of the seam, and fusinite, inertodetrinite, and semifusinite are identified in the entire seam. Inertodetrinite, fusinite, and semifusinite macerals are mostly observed within clay aggregates and densinite (Figures 4d and 5c-d), while individual fusinite and semifusinite macerals are also identified in the coal samples (Figure 5f). Funginite is less common in the coal samples and is mostly identified within ulminite (Figure 4c). Liptinite proportions show an increasing trend towards the upper part of the seam (Figure 3), which resulted in increased H contents. Cutinite, liptodetrinite and sporinite are identified in all the samples (Figures 4e-f). The presence of fluorinite-variety resinite could also imply the existence of *Myrica* within the palaeomire, which is also supported by the presence of *Myrica* pollen according to Türkmen et al. (2004). The identified minerals under white-incident light are mostly clay mineral aggregates and framboidal pyrite grains and agglomerates, and rarely syngenetic carbonate bands (Figures 4b-d, and 5c and f). Furthermore, calcareous fossil shell fragments and possible diatom remains and/or sponge spicules are also included (Figure 5e).

Table 2- Maceral composition (vol%) and mean random ulminite reflectance (%Rr) of the studied coal samples and floor sample (P-12) (TH: telohuminite, DH: detrohuminite, GH: gelohuminite, H: huminite, I: inertinite, L: liptinite, MM: mineral matter, Stdv: standard deviation).

Sample No	Petrographic Composition (vol%)							%Rr ± Stdv	Maceral Indices (dimensionless)						
	TH	DH	GH	H	I	L	MM		A	B	C	TPI	GI	VI	GWI
	vol%, on mineral-free basis						vol.%, on whole basis								
P-2	46.0	33.6	10.9	90.5	1.9	7.6	11.9		56.1	42.0	1.9	1.4	2.3	1.3	0.8
P-3	27.0	46.3	7.7	81.0	12.6	6.4	49.1		31.9	55.5	12.6	0.6	0.9	0.6	1.9
P-4	49.0	27.0	12.0	88.0	5.2	6.8	21.1	0.31±0.01	55.5	39.4	5.1	1.4	2.3	1.7	0.9
P-5	51.7	30.7	10.2	92.6	1.5	5.9	13.4		58.0	40.5	1.5	1.5	3.1	1.5	0.6
P-6	57.9	16.6	14.2	88.7	6.7	4.6	4.7	0.32±0.01	66.5	26.8	6.7	2.6	4.0	2.9	0.6
P-7	27.2	46.2	7.7	81.1	12.5	6.4	49.0		32.0	55.4	12.5	0.6	0.9	0.6	1.9
P-8	37.2	36.9	15.9	90.0	3.1	6.9	31.2	0.32±0.01	42.6	54.3	3.1	0.8	2.8	1.0	1.5
P-10	27.6	52.0	2.2	81.8	14.8	3.4	57.0	0.32±0.01	29.6	55.6	14.9	0.5	0.4	0.5	1.8
P-11	19.0	55.6	3.0	77.6	18.1	4.3	54.4		21.4	60.4	18.2	0.3	0.3	0.4	1.7
P-12	9.1	64.4	1.0	74.5	16.7	8.8	54.1		13.1	70.1	16.8	0.1	0.1	0.2	1.6

The mean random huminite reflectance (%Rr) values ranges between 0.31-0.32% (Table 2). These values are generally lower than the reported measured ones (0.38-0.51%) from the western part of the coalfield by Yalçın-Erik and Ay (2021).

4.3. Mineralogy

4.3.1. Minerals in Coal Samples

The minerals identified by XRD in the bulk coal samples, are calcite, clay minerals (illite and smectite),
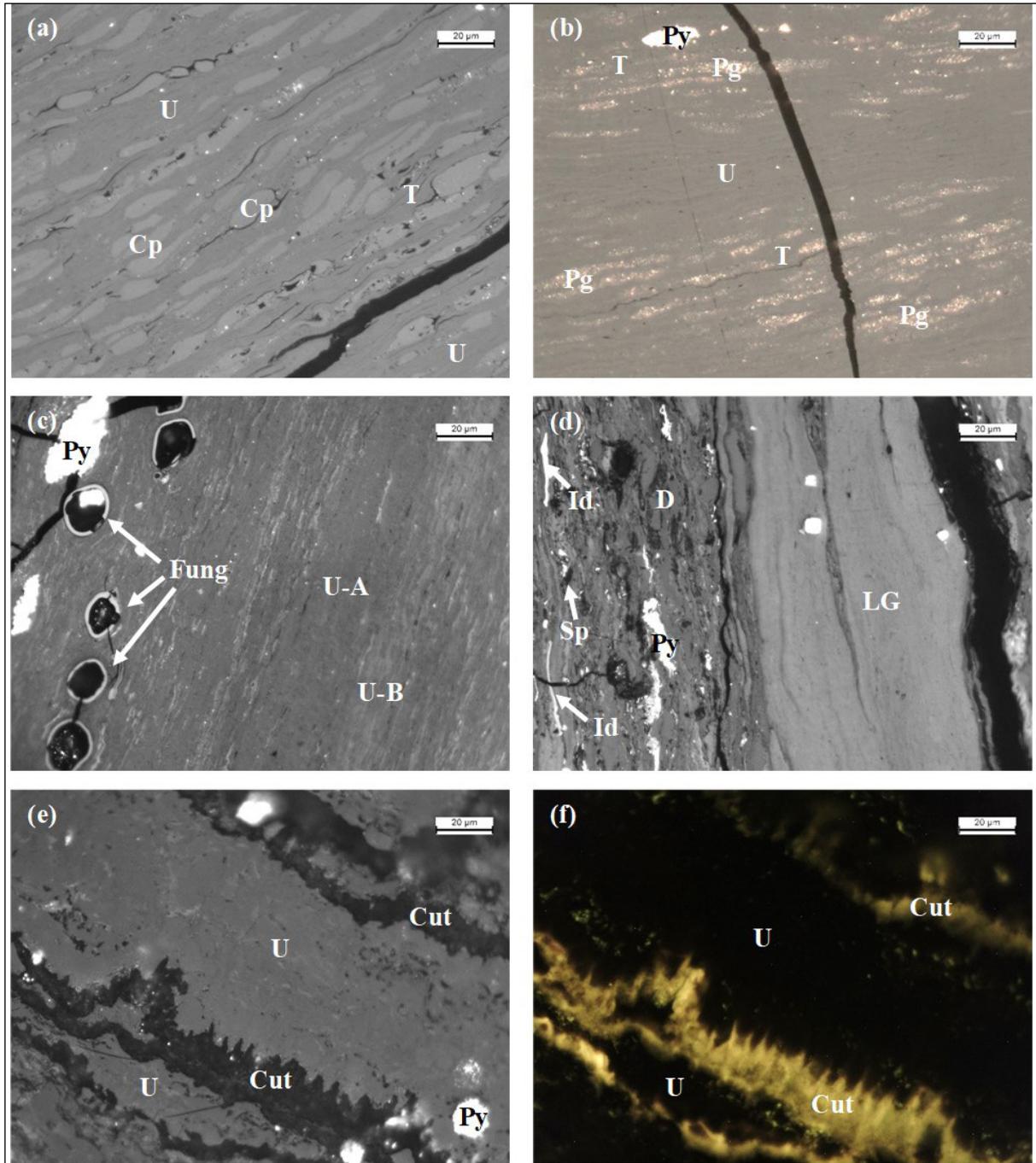
Figure 4- Selected photomicrographs of the Bozburun coal samples. All photomicrographs are taken under incident white light (a-e) or blue-light excitation (f), in oil immersion, 500× total magnification (Abbreviations: textinite (T), ulminite (U), ulminite-A (U-A), ulminite-B (U-B); densinite (D), corpohuminite (Cp), porigelinite (Pg), levigelinite (LG), inertodetrinite (Id), funginite (Fung); sporinite (Sp); cutinite (Cut), and pyrite (Py)).
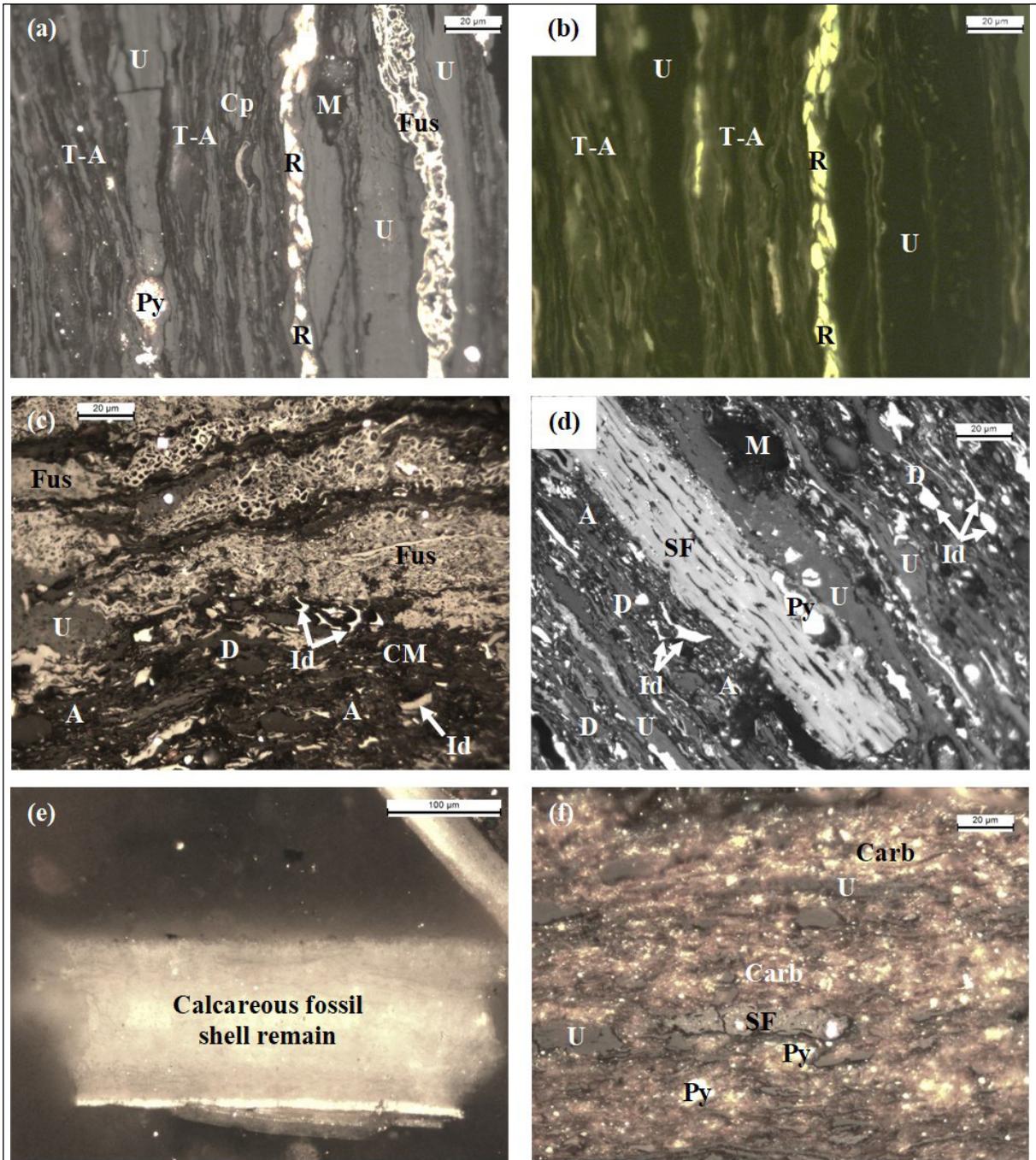
Figure 5- Selected photomicrographs of the Bozburun coal samples; a), c), d), e), f) all photomicrographs are taken under incident white light, b) blue-light excitation in oil immersion, 500× total magnification (Abbreviations: textinite-A (T-A), ulminite (U), attrinite (A), densinite (D), fusinite (Fus), semifusinite (SF), inertodetrinite (Id), resinite (R), pyrite (Py), clay mineral (CM), syngenetic carbonate (Carb), and mineral-matter (M)).

quartz, and pyrite (Table 3); a similar mineralogical composition is also obtained from the western part of the basin (Yalçın-Erik and Ay, 2021). Furthermore, in fossil shell-bearing samples, aragonite is also detected, and feldspars and marcasite are determined as minor phases (Table 3). Clay and carbonate minerals are

abundant to dominant phases, while quartz is generally a minor phase. The SEM-EDX data agrees with the XRD data, and chlorite (chamosite), Cl/F-apatite, celestine, dolomite, barite, sphalerite, titanite (sphen), and Ti-oxides, are identified as accessory phases (Table 3). In addition, pyritized calcareous fossil

Table 3- Semi-quantitative mineralogical composition of the Bozburun coal and non-coal samples based on XRD and SEM-EDX analyses (+++ = dominant phase (> 40%), ++ = abundant phase (10–20%), + = minor phase (< 10%) by XRD, a: accessory mineral detected by SEM-EDX).

Mineral	Sample											
	P-1	P-2	P-3	P-4	P-5	P-6	P-7	P-8	P-9	P-10	P-11	P-12
Quartz	+	+	+	+	+	+	+	+	+	+	+	+
Clay Minerals	+	+++	+++	+++	+++	+++	+++	+++	a	a	a	+++
Feldspar	a				+	a		a	a	a	a	+
Titanite	a					a						
Calcite	+++		+	++	++		+	+	+++	+++	+++	+
Aragonite			++		++						++	
Dolomite	a			a								
Pyrite	+	+++	++	++	++	+	+	+	+	a	+	+
Marcasite				a						+		
Sphalerite								a				
Celestine	a									a		
Barite	a											
Apatite						a			a	a		
Ti-oxides						a						

shell fragments and diatom/freshwater sponge spike remains, and fossil bone remains of Ca-phosphate composition were also identified using SEM-EDX.

4.3.2. Minerals in Non-coal Samples

According to XRD data, the minerals in the non-coal samples are similar to these of the coal samples. Calcite, clay minerals (smectite, illite and chlorite), quartz, and pyrite are identified in all non-coal samples (Table 3). Furthermore, feldspars are also detected from the floor sample. As expected, calcite is generally the dominant phase in the roof and parting samples in calcareous fossil remains-bearing samples, whereas in the floor sample clay minerals are predominant (Table 3). Quartz and pyrite are minor phases in the non-coal samples.

4.4. FT-IR Analysis

Selected FT-IR spectra are reported in Figure 6. The bands around wavenumbers 1030 and 530 cm⁻¹ could be originated from clay minerals (Georgakopoulos et al., 2003; Madejova, 2003). Furthermore, the intense bands at 3400 cm⁻¹ could also be attributed to clay minerals or more possibly with OH-stretching vibration (Madejova, 2003; Djowe et al., 2013; Jiang et al., 2021). The band around 470 cm⁻¹ could be attributed to quartz/silica grains (Çetinkaya and
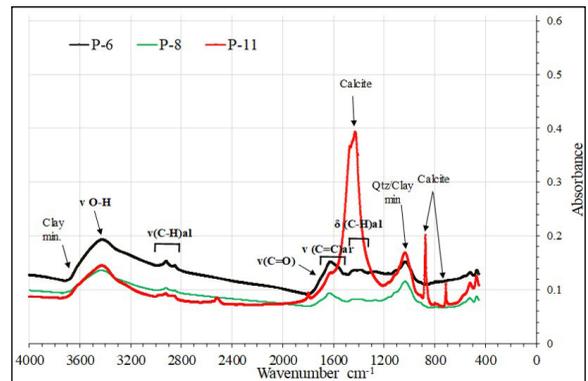
Figure 6- FT-IR spectra of selected Bozburun samples.

Yürüm, 2000; Georgakopoulos et al., 2003; Naik et al., 2021) however, the lack of intense bands at 1100 cm⁻¹ might not imply a lack of quartz/silica in the samples. This may be caused by the strong absorption of clay minerals and the overlap of quartz peak at 1100 cm⁻¹. Strong and board peaks around 1425, 875, and 711 cm⁻¹, particularly in the sample P-11, clearly result from calcite and/or fossil shell remains; similar peaks were also reported from fossil shell remains bands-bearing Turkish Neogene coals (e.g., Soma and Muğla Basins) (Çetinkaya and Yürüm, 2000; Baysal et al., 2016). The peaks at 2851 cm⁻¹ and 1385 cm⁻¹, and 2920 cm⁻¹ could imply the existence of aliphatic CH_2 and CH_3 symmetric and aliphatic C-H asymmetric

27

stretching vibrations, respectively (Oikonomopoulos et al., 2013; Chen et al., 2015; Jiang et al., 2021; Naik et al., 2021). The oxygen-containing functional groups (e.g., C=O and C=C aromatic ring) in coal samples could be evident with the peaks between 1613-1630 cm^{-1} (Georgakopoulos et al., 2003; Chen et al., 2015; Çelik et al., 2021).

4.5. Geochemistry

The major oxide contents of studied samples are reported in Table 4. The SiO$_2$ (8.4-46.8%, on whole coal basis) and Al$_2$O$_3$ (3.1-11.6%, on whole coal basis) contents of the coal samples are generally higher than inorganic samples. The CaO contents of fossil shell-bearing coal samples (34.5-37.6%, on coal basis) in the low part of seam, floor and intercalation samples (33.3-36.8%, on whole rock basis) are significantly higher than coal samples in the upper part of seam (1.5-6.0%, on whole coal basis) (Table 4). The contents of SiO$_2$, TiO$_2$, Al$_2$O$_3$, Na$_2$O, and K$_2$O display increasing trends towards the central part of the seam (Figure 7 and Table 4). As expected, the CaO content decreases towards the upper parts of the seam, and the Fe$_2$O$_3$ and MnO contents do not show any significant changes throughout the seam (Figure 7). The average concentrations of trace elements in analysed coal samples using ICP-MS do not exceed 100 ppm on a whole coal basis, except B and Sr concentrations (Tables 4 and 5). The average B concentration of coal samples is 161 ppm (Tables 4 and 5), whereas the average concentration of Sr is 1021 ppm, and the Sr concentration of sample P-10 is 6814 ppm on a whole coal basis (Tables 4 and 5). Like the coal samples, the average Sr concentration of non-coal samples exceeds 1000 ppm on a whole rock basis (Tables 4 and 6). In addition, the average Ba concentration of non-coal samples is higher than 100 ppm on a whole rock basis (Tables 4 and 6). The concentrations of trace elements in the coal samples are mostly less than 5 ppm, while the average concentrations of rare earth elements and Y (REY) contents do not exceed 1 ppm on a whole coal basis, except Y and La (Table 5).

The concentration coefficient (CC) of coal and non-coal samples was calculated for determining elemental enrichments (Tables 5 and 6). This calculation is based on dividing average concentrations of elements into Clarke values for low-rank coals and sedimentary rocks (Ketris and Yudovich, 2009; Dai et al., 2015b). Nickel (CC = 10.4) is the only significantly enriched element in coal samples, and the other enriched elements are Sr (CC = 8.5), As (CC = 5.8), Mo (CC = 5.4), and U (CC = 5.1). Furthermore, slightly enriched elements in coal samples are Cr (4.4), V (4.4), P (3.8), Ti (2.5), B (2.9), Rb (2.3), and Zn (2.1), whereas Ba and most of REY are depleted (CC<0.5) (Table 5). The remaining elements display concentrations close to the Clarke values of low-rank coals. In non-coal samples, the majority of elements are depleted (Table 6); nevertheless, the slightly enriched elements in non-coal samples are Sr (CC = 4.0), As (CC = 2.7), and Ni (CC = 2.2). The elements P, Ti, Cr, Mn, Co, Ba, Pb, and U have average concentration close to Clarke values of the sedimentary rocks (Table 6). Furthermore, outlook coefficient (C$_{outl}$) of REY and ΣREY oxides values of coal and non-coal samples are within non-promising for REY recovery potential (Seredin and Dai, 2012). Of note, the ashing temperature might also cause the volatization of As and B in coal samples; therefore, their CC might be higher than the measured concentrations.

5. Discussions

5.1. Coal Rank

The measured Rr values (0.31-0.32%) and the determined gross calorific values (6.7-28.8 MJ/kg, on dry, ash-free basis) of the coal samples imply that the Bozburun coal seam is of low rank C-B (lignite) according to ASTM D388-19a (2021), E.C.E-UN (1998) and ISO 11760 (2005) classifications. The coal samples are also classified as moderate to high ash yield coal and very low to moderate grade coal according to ISO 11760 (2005) and E.C.E-UN (1998) classification, respectively. Considering the ash yields of the mineral-rich lithotype samples from the low part of the seam, these samples could be classified as carbonaceous shale. Nevertheless, this identification could not be accurate since calcareous fossil shell remains-bearing bands are included in these samples.

In comparison with the reported measured Rr values (0.38-0.51%) from the western part of the Bozburun coalfield, and the northern part of the

Table 4- Elemental composition of coal and non-coal samples (all on whole rock-basis) in the Bozburun coalfield. All results in ppm, expect otherwise cited (LOI: loss on ignition, bdl: below detection limit).

Element	Sample											
	P-1	P-2	P-3	P-4	P-5	P-6	P-7	P-8	P-9	P-10	P-11	P-12
LOI (%)	31.0	72.4	55.1	70.6	70.7	81.6	26.7	60.6	37.2	38.7	37.0	37.0
SiO_2 (%)	21.7	12.9	22.7	11.8	11.0	8.4	46.8	22.1	15.1	10.7	15.4	33.1
TiO_2 (%)	0.2	0.3	0.3	0.2	0.2	0.2	0.7	0.4	0.1	0.2	0.2	0.7
Al_2O_3 (%)	5.9	4.0	6.3	3.3	3.1	2.2	11.6	5.6	4.3	3.1	4.7	10.9
Fe_2O_3 (%)	3.4	5.5	6.3	5.6	5.5	3.3	5.8	6.3	2.4	6.1	4.6	6.7
MnO (%)	0.11	0.05	0.07	0.06	0.07	0.04	0.08	0.07	0.09	0.09	0.07	0.09
MgO (%)	2.6	2.2	2.8	2.1	2.2	1.7	3.6	2.4	2.7	2.1	2.0	4.3
CaO (%)	33.3	1.5	4.8	5.1	6.0	1.4	2.2	1.0	36.8	37.6	34.5	4.3
Na_2O (%)	0.4	0.6	0.7	0.6	0.6	0.6	0.8	0.7	0.3	0.3	0.3	0.9
K_2O (%)	1.2	0.4	0.7	0.4	0.4	0.4	1.5	0.8	0.8	0.7	1.0	1.8
P_2O_5 (%)	0.12	0.12	0.22	0.22	0.25	0.18	0.07	0.06	0.13	0.28	0.15	0.13
Li	bdl	10	12	6.0	7.2	5.5	14	14	bdl	bdl	bdl	8.4
B	15	216	146	234	235	297	87	170	17	37	28	30
Sc	3.4	2.6	2.9	2.2	2.6	2.2	7.6	4.5	2.2	2.1	2.4	5.9
V	20	70	142	81	89	110	82	152	21	69	74	43
Cr	63	57	66	45	55	47	126	104	41	45	49	108
Co	4.1	8.9	8.0	3.7	3.5	3.6	14	12	3.1	5.4	5.5	15
Ni	43	103	153	55	64	40	142	147	31	70	68	166
Cu	7.5	8.3	14	11	9.8	10	13	11	8.0	13	12	15
Zn	21	37	24	22	26	23	94	59	17	26	33	84
Ga	bdl	4.2	4.9	4.0	4.0	2.7	7.6	6.0	bdl	4.2	bdl	6.8
As	23	22	66	75	115	12	19	35	10	33	18	29
Rb	15	12	20	15	15	11	66	26	18	16	22	68
Sr	1794	244	239	329	269	240	162	216	1218	6813	679	244
Y	3.6	2.2	3.5	2.2	2.3	5.4	8.5	5.5	3.0	2.7	3.6	5.3
Cd	bdl	bdl	bdl	bdl	1.7	0.9	bdl	bdl	bdl	bdl	bdl	bdl
Mo	bdl	14.7	8.9	16.1	16.1	19.5	4.8	13.6	bdl	6.6	7.4	bdl
Sb	bdl	bdl	6.6	bdl	bdl	bdl	bdl	bdl	bdl	bdl	bdl	bdl
Ba	478	32	33	33	26	16	56	35	126	181	97	47
La	4.6	3.1	5.3	3.1	3.6	4.7	16	6.6	3.2	3.0	4.5	13
Ce	8.5	6.5	11	5.6	6.3	7.9	30	12	5.6	5.4	7.8	24
Pr	1.1	0.7	1.3	0.7	0.8	1.0	4.0	1.6	0.7	0.7	1.0	3.2
Nd	3.5	2.4	4.2	2.2	2.6	3.5	13	5.0	2.4	2.4	3.4	10
Eu	0.3	0.1	0.2	0.1	0.1	0.2	0.7	0.3	0.2	0.2	0.2	0.4
Gd	0.7	0.4	0.8	0.4	0.5	0.8	2.3	1.1	0.6	0.5	0.7	1.9
Tb	0.14	0.08	0.13	0.09	0.09	0.15	0.4	0.2	0.06	0.06	0.12	0.3
Dy	0.6	0.4	0.7	0.3	0.4	0.7	1.8	1.0	0.4	0.4	0.6	1.3
Ho	0.14	0.08	0.13	0.09	0.09	0.16	0.3	0.2	0.06	0.06	0.12	0.3
Er	0.3	0.2	0.4	0.2	0.2	0.4	0.8	0.6	0.2	0.2	0.3	0.4
Tm	bdl	bdl	bdl	bdl	bdl	0.07	0.14	0.08	bdl	bdl	bdl	0.08
Yb	0.3	0.2	0.3	0.2	0.2	0.4	0.6	0.5	0.2	0.2	0.2	0.5
Lu	bdl	bdl	bdl	bdl	bdl	0.05	0.07	0.08	bdl	bdl	bdl	bdl
Hf	2.0	1.3	1.0	0.9	1.3	0.7	1.7	2.9	bdl	0.8	0.6	1.4
Pb	bdl	6.1	bdl	3.7	5.8	4.5	14.4	10.8	bdl	bdl	9.2	16.9
Th	1.6	1.9	2.8	1.3	1.6	1.3	6.9	3.3	1.1	1.0	1.4	5.7
U	0.7	10.9	15.5	16.7	19.6	20.4	9.5	19.2	2.0	9.8	10.0	4.4
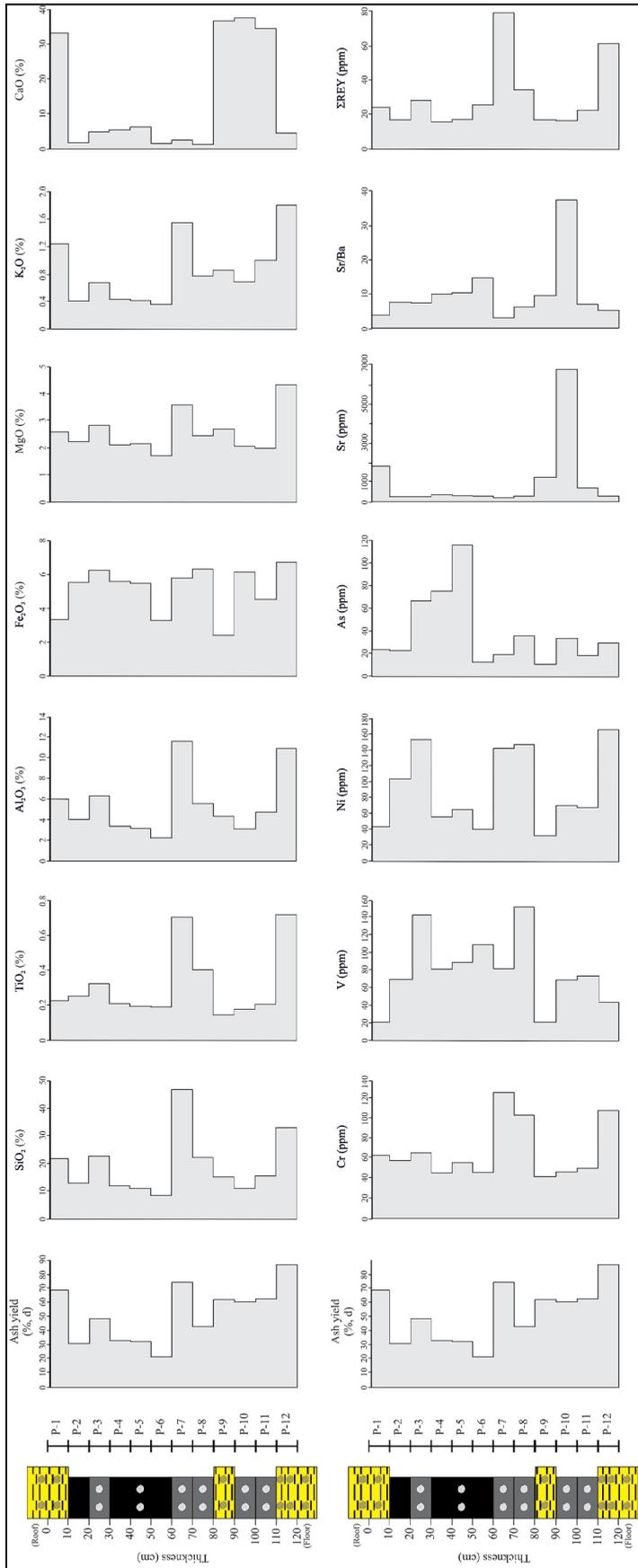
Figure 7- Vertical distribution of; a) SiO_2, TiO_2, Al_2O_3, Fe_2O_3, MgO, K_2O, CaO and b) Cr, V, Ni, As, Sr, ΣREY and Sr/Ba ratio through the studied seam (for lithostratigraphic column, see Figure 2).

Table 5- Weighted average of the Ti, P, Mn, minor and trace elements (in ppm) for the Bozburun coal samples and their comparison with worldwide coals (a: from Swaine (1990); b: from Ketris and Yudovich (2009). Elements in bold are enriched.

Element	Most world coals[a]	Clarke values for low-rank coals	Bozburun coal samples	Concentration coefficient (CC)
Li	1-80	10	7.7	0.8
B	**5-400**	**56**	**161**	**2.9**
P	**10-3000**	**200**	**757**	**3.8**
Sc	1-10	4.1	3.2	0.8
Ti	**10-2000**	**720**	**1769**	**2.5**
V	**2-100**	**22**	**96**	**4.4**
Cr	**0.5-60**	**15**	**66**	**4.4**
Mn	**5-300**	**100**	**517**	**5.2**
Co	0.5-30	4.2	7.2	1.7
Ni	**0.5-50**	**9.0**	**94**	**10.4**
Cu	0.5-50	15	11	0.8
Zn	**5-300**	**18**	**38**	**2.1**
Ga	1-20	5.5	4.2	0.8
As	**0.5-80**	**7.6**	**44**	**5.8**
Rb	2-50	10	23	2.3
Sr	**15-500**	**120**	**1021**	**8.5**
Y	2-50	8.6	4.0	0.5
Cd	0.1-3	0.24	0.3	1.2
Mo	**0.1-10**	**2.2**	**12**	**5.4**
Sb	0.5-10	0.84	0.7	0.9
Ba	20-100	150	57	0.4
La	1-40	10	5.6	0.6
Ce	2-70	7.2	10	1.4
Pr	1-10	3.5	1.3	0.4
Nd	3-30	11	4.3	0.4
Eu	0.1-2	0.5	0.2	0.5
Gd	0.1-4	2.6	0.8	0.3
Tb	0.1-1	0.32	0.1	0.5
Dy	1-4	2.0	0.7	0.3
Ho	0.1-2	0.5	0.1	0.3
Er	1-3	0.85	0.4	0.4
Tm	0.5-3	0.31	0.0	0.2
Yb	0.3-3	1.0	0.3	0.3
Lu	0.03-1	0.19	0.02	0.1
Hf	0.4-5	1.2	1.2	1.0
Pb	2-80	6.6	6.1	0.9
Th	0.5-10	3.3	2.4	0.7
U	**0.5-10**	**2.9**	**15**	**5.0**

Table 6- Weighted average of the Ti, P, Mn, minor and trace elements (in ppm) for the Bozburun non-coal samples and their comparison with worldwide coals [a: from Ketris and Yudovich (2009)].

Element	Clarke values for sedimentary rocks[a]	Bozburun non-coal samples	Concentration coefficient (CC)
Li	33	2.8	0.1
B	72	20	0.3
P	670	567	0.8
Sc	9.6	3.8	0.4
Ti	3740	2180	0.6
V	91	28	0.3
Cr	58	71	1.2
Mn	830	755	0.9
Co	14	7.4	0.5
Ni	**37**	**80**	**2.2**
Cu	31	10	0.3
Zn	43	41	0.9
Ga	12	2.3	0.2
As	**7.6**	**20.7**	**2.7**
Rb	94	33.4	0.4
Sr	**270**	**1085**	**4.0**
Y	29	4.0	0.1
Ba	410	217	0.5
La	32	6.8	0.2
Ce	52	13	0.2
Pr	6.8	1.7	0.2
Nd	24	5.4	0.2
Eu	0.94	0.3	0.3
Gd	4	1.1	0.3
Tb	0.69	0.2	0.3
Dy	3.6	0.8	0.2
Ho	0.92	0.2	0.2
Er	1.7	0.3	0.2
Tm	0.78	0.03	0.0
Yb	2	0.3	0.2
Hf	3.9	1.1	0.3
Pb	12	5.6	0.5
Th	7.7	2.8	0.4
U	3.4	2.4	0.7

Malatya Basin (0.68-0.79%) (Karayiğit and Whataley, 1997; Yalçın-Erik and Ay, 2021), the studied samples generally display relatively low Rr values (Table 3). Furthermore, the calculated Rr values using Rock-Eval pyrolysis data obtained from the western part of the Bozburun coalfield and coal beds outcropping north of Arguvan town (Yalçın-Erik and Ay, 2021), strongly vary from 0.20-0.69%. This parameter is proposed for organic-rich rock and/or bituminous shale samples by Jarvie et al. (2001), and its application to humic coals, particularly on Cenozoic low-rank coals, could be very problematic due to the presence of certain compounds (Zdravkov et al., 2006; Hazra et al., 2019; Çelik et al., 2021). For instance, the oxygenated functional groups in ulminite macerals (e.g., ulminite A or resin-impregnated ulminite A) or the breakdown of carbonate minerals could elevate S_3 peak values; hence, the T_{max} values are suppressed and calculated Rr values could be reduced. Considering the presence of oxygen-containing functional groups in the FT-IR spectra and the carbonate minerals in the coal samples, the calculated Rr values from Rock-Eval pyrolysis data should be used with caution as a rank parameter for the Bozburun coal. As mentioned above, the presence of H-rich compounds could also cause a reduction of the Rr values. The reported palynological and biomarker datasets from the Bozburun coalfield imply the existence of H-rich peat-forming plants (e.g., Taxodaecae-Cupressecae) within the palaeomire (Önal, 1995; Türkmen et al., 2007; Yalçın-Erik and Ay, 2021). Thus, significantly low Rr values (e.g., 0.27) were calculated from coals according to Rock-Eval data. Nevertheless, the coal petrography data indicates that the potential influence of H-rich ulminite macerals on Rr values may be very limited, because ulminite B is the dominant telohuminite and ulminite A in the studied samples displays very weak fluorescence only (Figure 5b).

Another possibility controlling Rr differences within the Malatya Basin could be the tectonic deformation. Since the study area faced post-coalification regional tectonic deformation, the Rr values might have been affected (Hower and Gayer, 2002). This also seems to be not possible due to the lack of any deformed macerals in the coal samples. In the northern part of Malatya Basin, Pliocene basalts and andesitic domes of the Yamadağ volcanics are widely exposed and overlay late Miocene coal-bearing sequences (Karayiğit and Whateley, 1997; Ekici et al., 2007). The measured Rr values of the coal seams in the Selimoğlu coalfield are around 0.70%, which indicates bituminous rank. Nevertheless, the elevated measured Rr values are obviously controlled by heat flow due to post-coalification andesitic domes in the Selimoğlu coalfield (Karayiğit and Whateley, 1997). Considering the presence of Pliocene volcanic rocks and lavas north of Arguvan town, the reported slightly high calculated Rr values of the coal beds outcropping in this area (Kuyudere and Akören locations in Figure 1a), could be related to increased heat flow in the northern part of Malatya Basin (Yalçın-Erik and Ay, 2021).

Since the Pliocene volcanic rocks are observed in the Bozburun coalfield, the relative differences on measured Rr values among the coalfield may not be related to influence of heat flow, like in the northern part of the Malatya Basin. Nevertheless, alkaline conditions within the palaeomire could cause biogeochemical gelification of organic matter; in turn, high gelification degree of organic matter could result in an increase of the Rr values (Dehmer, 1995). As can be seen in sections 5.2 and 5.4, gelification index (GI) values are different within the coalfield and carbonate minerals are more common in the western part of the Bozburun coalfield, the studied section and the western part of the Bozburun coalfield display relatively small Rr differences due to biogeochemical gelification and alkaline conditions within the palaeomire. Overall, coal-rank variations were developed from the northern (Selimoğlu coalfield) to the southern part (Bozburun coalfield) of the Malatya Basin due to post-coalification volcanic activity; biogeochemical gelification within the palaeomires caused variations in Rr values within the Bozburun coalfield.

5.2. Provenance of minerals

Quartz/silica is mostly identified as irregularly shaped individual grains during SEM-EDX examination (Figure 8a and d), which indicates a clastic origin. In some samples, partially pyritized siliceous skeletons of diatoms and/or sponge spicules are also detected (Figure 8e). Such remains suggest
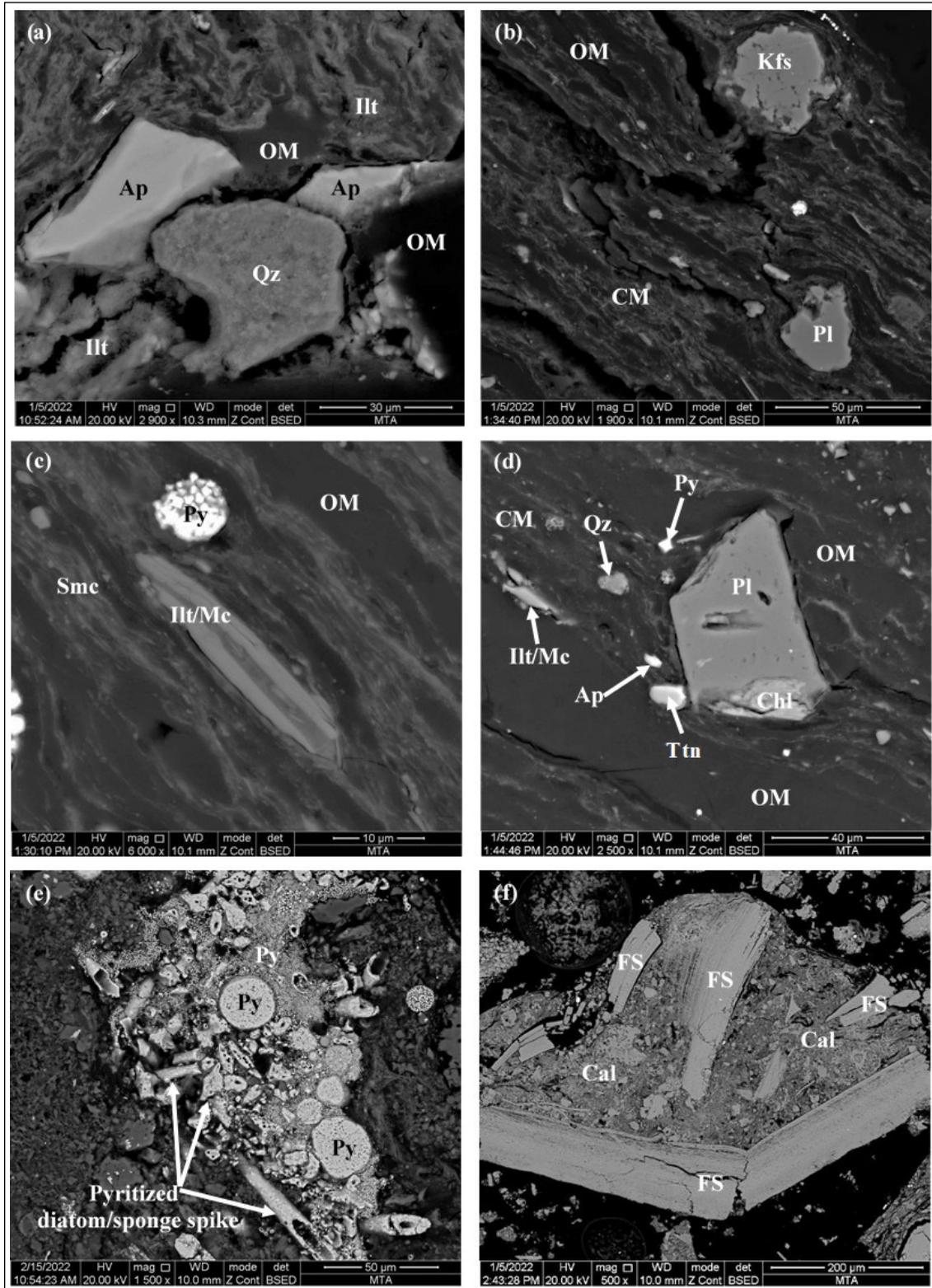
Figure 8- Selected SEM backscattered (BSE) images from the Bozburun samples: a) apatite (Ap), quartz (Qz) and organic matter (OM) associated with illite (Ilt), b) K-feldspar (Kfs), plagioclase (Pl) and organic matter associated with clay minerals (CM), c) illite/mica (Ilt/Mc) and organic matter associated with smectite (Smc) and framboidal pyrite (Py) grain, d) apatite (Ap), chlorite (Chl), quartz (Qz), plagioclase (Pl), titanite (Ttn), illite/mica (Ilt/Mc) and organic matter (OM) associated with clay minerals (CM), e) pyritized possible diatom/sponge spike and framboidal pyrite (Py) aggregates, f) calcite (Cal) and fossil shell remains (FS).

that silica in coal samples is also biogenic in origin (Ward, 2002; Oskay et al., 2016; Çelik et al., 2021). Even though feldspar is a minor phase, K-feldspar and plagioclase grains are commonly observed during the SEM-EDX study. Like quartz, feldspar grains are identified as irregular shaped individual grains with sharp edges within clay mineral aggregates (Figure 8b and d). This implies short-distance transport of feldspar grains from the adjacent areas. The clastic sources for feldspars presumably are mainly the middle Miocene Malatya volcanics, and, in a lesser extent, the late Cretaceous Elazığ magmatics of the basements.

Clay minerals are identified as aggregates hosting also other mineral grains (e.g., Cl/F-apatite, quartz, feldspars, and titanite) and organic matter (Figures 8a-d). The clay aggregates mostly consist of smectite and subordinately illitic according to the SEM-EDX data. Illite components mostly derive as clastic input into the palaeomire (Siavalas et al., 2009), while smectite mostly originates from alteration of syngenetic or epiclastic volcanic input (Bohor and Triplehorn, 1993; Dai et al., 2017, 2020a; Karayiğit et al., 2020b). Since illitic aggregates are more common in the low part of the seam, illite aggregates in samples are syngenetic and clastic in origin. Furthermore, the individual illite/mica grains in the clay matrices could also be related to clastic input from the middle Miocene Malatya volcanic and/or magmatic rocks in the pre-Neogene basement (Figures 8c-d). The alterations of clastic input from the Malatya volcanics within the mires could result in syngenetic smectite formation under hydrogeologically closed system. During the SEM observations, lath-shaped Fe-rich chlorite (chamosite) grains are generally observed within the clay aggregates. Also, chlorite overgrowths are detected around feldspar grains (Figure 8d). These could indicate that chlorite is either derived from clastic inputs into palaeomires or alteration of feldspar grains within the paleomires and/or early diagenetic stages (Ward, 2002; Hower et al., 2015).

Carbonate minerals generally appear in form of carbonate bands and calcareous fossil shell remains, and rarely as individual calcite and dolomite grains (Figures 8f, 9a-b). These observations might imply

that the carbonates are clearly syngenetic originating from clastic input from the Permo-Triassic Keban metamorphics (e.g., marbles) or the pre-Neogene carbonates. Besides, calcareous fossil fragments, which are partially pyritized, are commonly observed in fossil shell remains-bearing samples (Figures 9a-b). Aragonite is generally detected as an abundant phase in the XRD patterns in a few fossil shell remains-bearing samples. However, aragonite was not detected in some calcareous fossil remains-bearing samples, whilst calcite is detected instead of aragonite (Table 3). This could be related to the conversion of aragonite to its polymorph calcite within the palaeomire or during a diagenetic stage (Querol et al., 1999; Ward, 2002). The predominance of carbonate minerals and the presence of partially pyritized calcareous fossil shell remains could indicate neutral to weak alkaline conditions (Kortenski, 1992; Karayiğit et al., 2017a;). However, the lack of carbonate minerals and the existence of framboidal pyrite grains and siliceous fossil remains (e.g., diatom) in the upper seam part point to low pH values of mire water or the Ca contents of influenced water into palaeomires was decreased (Korstenski, 1992; Dai et al., 2020a). Thus, syngenetic carbonate formation was limited due to increased acidity of palaeomire during late stages of peat accumulation in the Bozburun coalfield. Overall, syngenetic carbonate formation in the Bozburun palaeomire was controlled by the Ca-rich water influx along with clastic influx.

Pyrite is generally observed as individual framboidal aggregates within organic matter (e.g., ulminite), and framboidal and euhedral pyrite grains aggregate during coal petrography and SEM studies (Figures 4b, c, e, 5a, f, 8c, e, 9a). Additionally, cleat/fracture pyrite-infillings, and pyritized plant tissues, siliceous skeletons of diatoms and/or sponge spicules, and fossil shell remains, as mentioned above, are contained in coal samples (Figure 8e, f, 9c). These findings suggest that framboidal pyrite grains were precipitated within the palaeomire and/or early diagenetic stages as a result of sulphate-reducing bacteria and sulphate-rich water influx into palaeomires (Querol et al., 1989). The cleat/fracture pyrite-infillings are presumably controlled by precipitation of sulphate-rich porewaters during coalification. Another sulphide mineral identified by XRD is
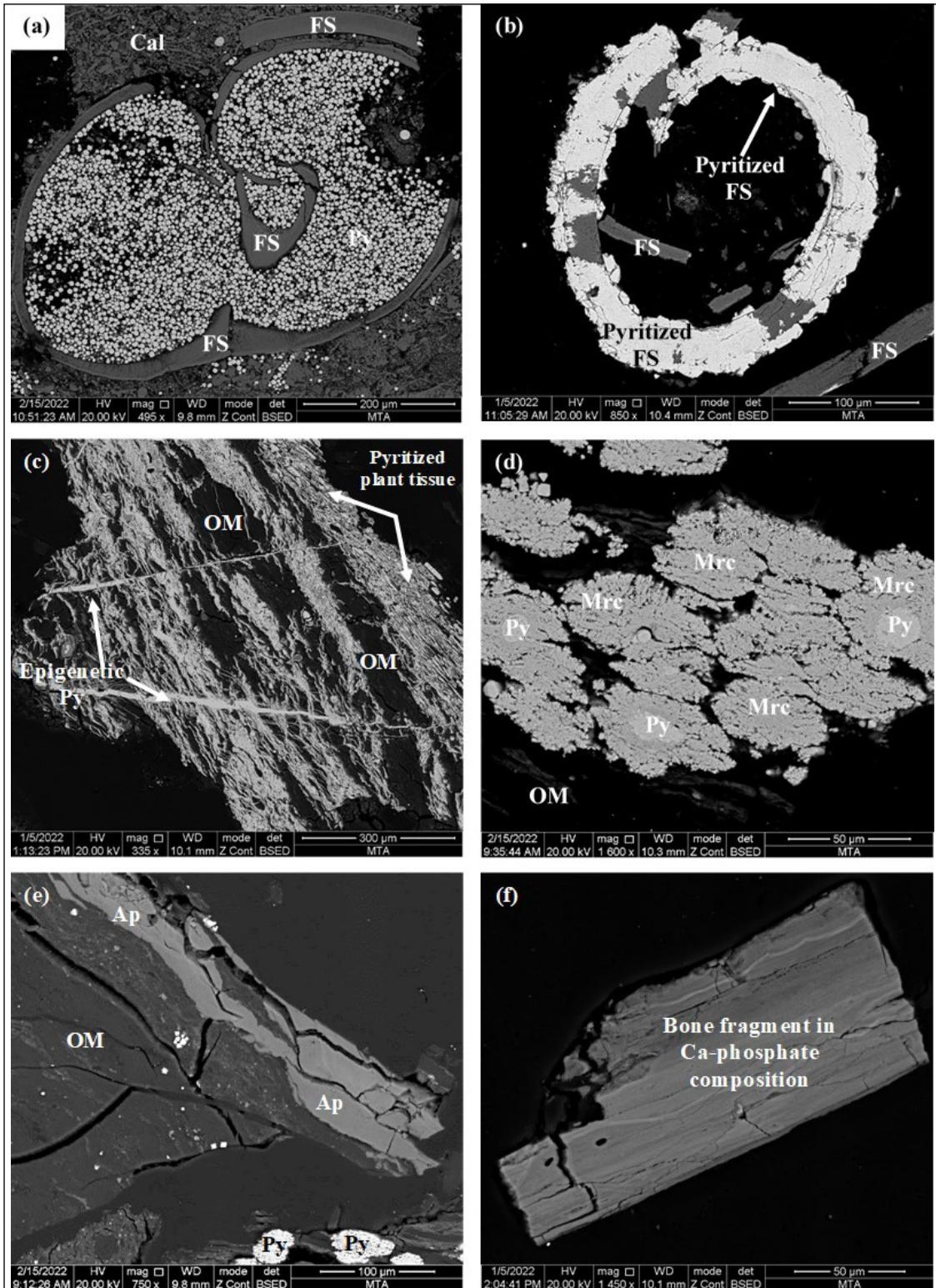
Figure 9- Selected SEM-BSE images from the Bozburun samples: a) calcite (Cal), fossil shell remains (FS) and euhedral pyrite grains, b) fossil shell remains (FS) and pyritized fossil shell remain, c) marcasite (Mrc) overgrowths around framboidal pyrite (Py) grains within organic matter (OM), d) epigenetic cleat/fracture pyrite infillings (Py) with organic matter and pyritized plant tissue, e) cleat/fracture apatite infillings (Ap) within organic matter (OM) and framboidal pyrite (Py) grains and f) fossil bone remain in Ca-phosphate composition.

marcasite (Table 3), and dendritic-like marcasite was identified as overgrowths around framboidal nucleated pyrite grains in a few samples by SEM-EDX (Figure 9d). Marcasite in coal is sometimes thought to be an indicator of marine influence in palaeomires and/or hydrothermal solution penetration (Querol et al., 1989; Rieder et al., 2007); however, both cases can be ruled out based on palaeontological data from the seam and the lack of cleat/fracture marcasite-infillings. Marcasite overgrowths around nuclei of framboidal pyrite grains; on the other hand, it forms replacing early diagenetic framboidal pyrite grains during the late diagenetic stages (Querol et al., 1989; Ruppert et al., 2005; Kolker, 2012). For such marcasite formation, pH should be lower than 5.0 (Ruppert et al., 2005); despite the fact that the co-existence of syngenetic pyrite grains and carbonate bands in these samples could indicate that marcasite formation was developed under weak acidic to neutral conditions. Other sulphide mineral that was identified by SEM-EDX in coal samples is sphalerite (Table 3), and its presence within clay mineral aggregates indicates a clastic origin. These micron-sized sphalerite grains are presumably derived from volcanic and/or magmatic rocks in the adjacent areas as clastic inputs into the palaeomire.

Apatite is the only identified phosphate mineral in the Bozburun coalfield by SEM-EDX, and apatite grains are identified within the clay mineral aggregates and/or syngenetic carbonate bands (Figures 8a, d, 9e, f, 10a), which indicate detrital origin for apatite. The presence of measurable Cl, F, and Sr (Figure 10a) in these grains could also imply that apatite grains have volcanogenic origin (Bohor and Triplehorn, 1993; Dai et al., 2020a). Beside individual apatite grains, cleat/fracture apatite-infillings (Figure 9e) and Ca-phosphate fossil bone remains (Figure 9f) are also observed during SEM-EDX analysis in a few samples. Cleat/fracture apatite-infillings are mostly derived from reactions between liberated P from decay of plant matter and dissolved CaO in porewater during coalification, while Ca-phosphate fossil bone remains are related to biogenic activities within the palaeomire (Ward, 2002). Hence, apatite has both syngenetic (clastic and biogenic) and epigenetic origin.

The identified sulphate minerals in the samples are barite ($BaSO_4$) and celestine ($SrSO_4$). Celestine grains are identified as euhedral individual grains within the syngenetic carbonate bands in coal samples and roof rock samples (Figure 10b-f). In addition, individual euhedral barite grains and barite-celestine (Ba, $SrSO_4$) solid solution overgrowths associated with syngenetic carbonate bands and rarely feldspar grains are also observed in the roof sample (Figure 10e-f). Barite is a common sulphate mineral in coal, while celestine in coal is less common. Both sulphate minerals generally originate from the precipitation of sulphate-rich solutions during coalification and/or leached solutions overlying marine sediments, and syngenetic barite in coal seams is very rare (Finkelman et al., 2019; Dai et al., 2020a, 2021; Karayiğit et al., 2020a). The authigenic formation of celestine is generally related to evaporation of seawater or reactions between Sr-bearing hypersaline fluids with gypsum/anhydrite (Honar, 2004). However, the identified mollusc fauna from the Bozburun coalfield implies freshwater to oligohaline conditions during the late Miocene. Therefore, any influence of marine and/or hypersaline water influence on the palaeomire and/or onset of geochemical coalification could be ruled out for the study area. Celestine and Sr-bearing barite have been found within cavities of syngenetic framboidal pyrite grains in Turkish Neogene coals, as well as Sr-bearing barite overgrowths around feldspars (e.g., Kangal/Sivas and Keles and Orhaneli/Bursa) (Karayiğit et al., 2019, 2021; Çelik et al., 2021). In these coalfields, altered tuff layers are located in the coal seams, and liberated Sr and Ba from alteration of volcanogenic minerals (e.g., Sr-/Ba-bearing feldspars) and/or air-fall ash (tephra) within paleomires were reacted with sulphuric acid in the palaeomire. As a result of sulphate-reducing bacteria activity in the palaeomire, celestine and Sr-bearing barite were precipitated along with syngenetic framboidal pyrite grains. Furthermore, the geochemical data from the Yamadağ volcanic complex reported high Ba and especially high Sr contents of Miocene andesite and basalt (Kocaaslan and Ersoy, 2018; Di Giuseppe et al., 2021). In the roof rock samples, the presence of barite grains and overgrowth barite-celestine solid solution associated with feldspar grains could explain the source of Ba and Sr in the roof rock samples. The presence of Sr-
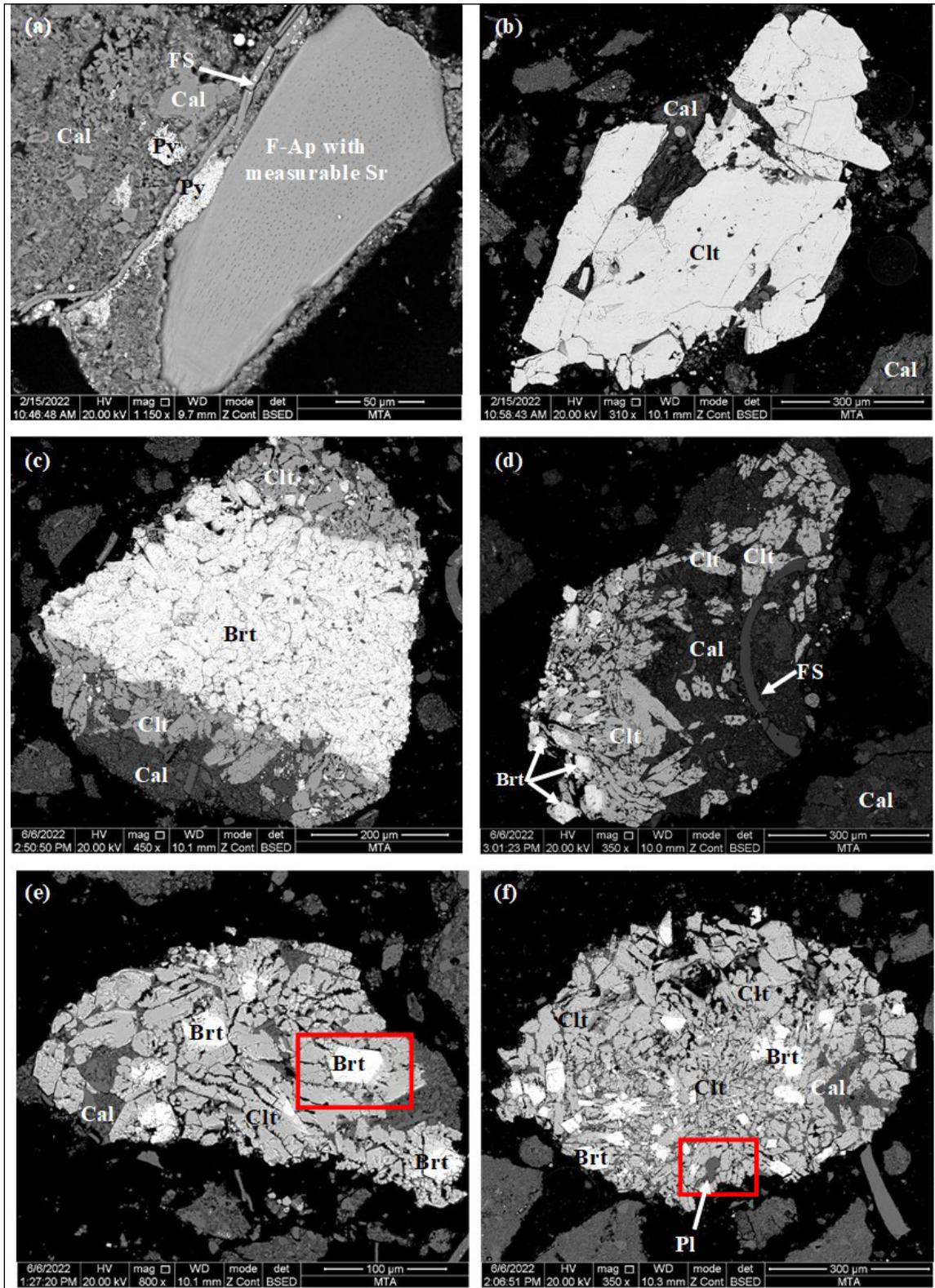
Figure 10- Selected SEM-BSE images from the Bozburun samples; a) fluorapatite (F-Ap) with measurable Sr and fossil shell (FS) remains within syngenetic carbonate bands (Cal) and framboidal pyrite (Py) grains, b) authigenic celestine (Clt) grains and syngenetic carbonates (Cal), c), f) celestine (Clt) and barite (Brt) within syngenetic carbonates and clastic plagioclase (Pl) grains and fossil shell (FS) remains. (Highlighted area in images e and d are reported in Figures 13 and 14, respectively).

bearing volcanogenic apatite grains could be another evidence of a clastic volcanogenic mineral source for Sr in the samples. Even though Ba and Sr could be derived from alteration of volcanogenic minerals in the Bozburun palaeomire, no altered tuff layer was identified in the coal seam and/or volcanic rocks were not observed from the overlying units in the coalfield. Therefore, the necessary Ba and Sr ions should have derived from another main source instead of clastic feldspar grains from middle Miocene volcanic rocks in the basin.

Economic gypsum and celestine deposits are found in late Cretaceous, Eocene, and early Miocene marine carbonates in the neighbouring Sivas Basin (Tekin et al., 2002). Similarly, Palaeogene-late Eocene marine carbonates in the basement rocks of the Malatya Basin contain gypsum layers and lenses like those in the Sivas Basin (Sümengen, 2016). Strontium is more soluble in aquatic environments than Ba (Hanor, 2004), and additional Sr could be introduced into the Bozburun palaeomire by dissolved sulphate-rich water from the gypsum-bearing Palaeogene-late Eocene marine carbonate. Therefore, alteration of clastic Ba-and Sr-rich feldspars from the middle Miocene Malatya volcanics and/or sulphate-rich water influx from the gypsum-bearing pre-Neogene units could be a source for Ba and Sr ions in the Bozburun palaeomire. Besides, Sr could display a high concentration in aragonitic mollusc shells, and this element could be essential for biogenic aragonite precipitation in the aquatic system (Hanor, 2004; Böning and Bard, 2009; Brisset et al., 2017) as well as Sr-bearing calcareous fossil shell remains were reported from some Turkish Neogene coalfields (Karayiğit et al., 2000). Hence, introduced Sr from alteration of clastic feldspar grains in the palaeomire and/or sulphate-rich water influx could be uptaken by molluscs. With this assumption, a measurable amount of Sr should be traced by SEM-EDX from calcareous fossil shell remains in the studied samples. During the SEM-EDX observation, Sr was rarely detected from these remains (Figure 11); nevertheless, Sr could also be released from aragonitic fossil shell remains during calcination in the depositional environment at an early diagenetic stage (Querol et al., 1999; Hanor, 2004; Marcano et al., 2015). Furthermore, Sr could not be incorporated

into calcite due to its bigger ionic radius than this of Ca^{2+} (Langston et al., 1998; Finch and Allison, 2008). Thus, liberated Sr ions from calcination of fossil remains also seem having reacted with dissolved sulphate ions in the mire water. Overall, authigenic barite and celestine, and barite-celestine solid solution formation took place during diagenetic stages.

5.3. Factors Controlling the Elemental Distribution

The statistical approach is commonly applied for determining mode of occurrence of elements in coal (Dai et al., 2021). Nevertheless, recent studies denoted that the statistical approach should be cooperated with SEM-EDX or other direct methods in order to eliminate misinterpretations (Dai et al., 2021; Xu et al., 2022; Eminağaoğlu et al., 2022). Therefore, both statistical and SEM-EDX analyses were here applied in order to accurately identify the controlling factors of elemental distribution. The major oxides, such as SiO_2, TiO_2, MgO, and K_2O, display positive correlations with ash yield and Al_2O_3 content (Table 7); which indicates aluminosilicate mineral affinity. The SEM-EDX data also agrees with this observation, and the contents in TiO_2, MgO, K_2O, and Na_2O are determined from clay minerals. Besides clay minerals, feldspar grains in the samples are another source of K_2O and Na_2O. In addition, Al_2O_3 contents of the samples show positive correlations with elements like Ga, Rb, Ni, and the REY (Table 7), which also imply an aluminosilicate affinity. Since aluminosilicate minerals in the samples are clastic in origin, clastic influx from volcanic and metamorphic rocks into the palaeomire could control their distributions and enrichment. This might also explain why P_2O_5 concentrations are high in clastic apatite-bearing samples (Figures 8a and 10a, and Table 4). Additionally, measurable Mg is also determined from fossil shell fragments (Figure 11). Furthermore, TiO_2 displays a moderate positive correlation with Fe_2O_3, which could be related to the accessory Ti-oxide and/or titanite in the samples (Figure 8d). The lack of correlation among Fe_2O_3, ash yield, total S, Al_2O_3, and SiO_2 contents could imply an intermediate affinity for Fe_2O_3; however, Fe is also detected in clay minerals, sulphides, and sulphates in the samples. Therefore, iron seems having an inorganic affinity in the samples.
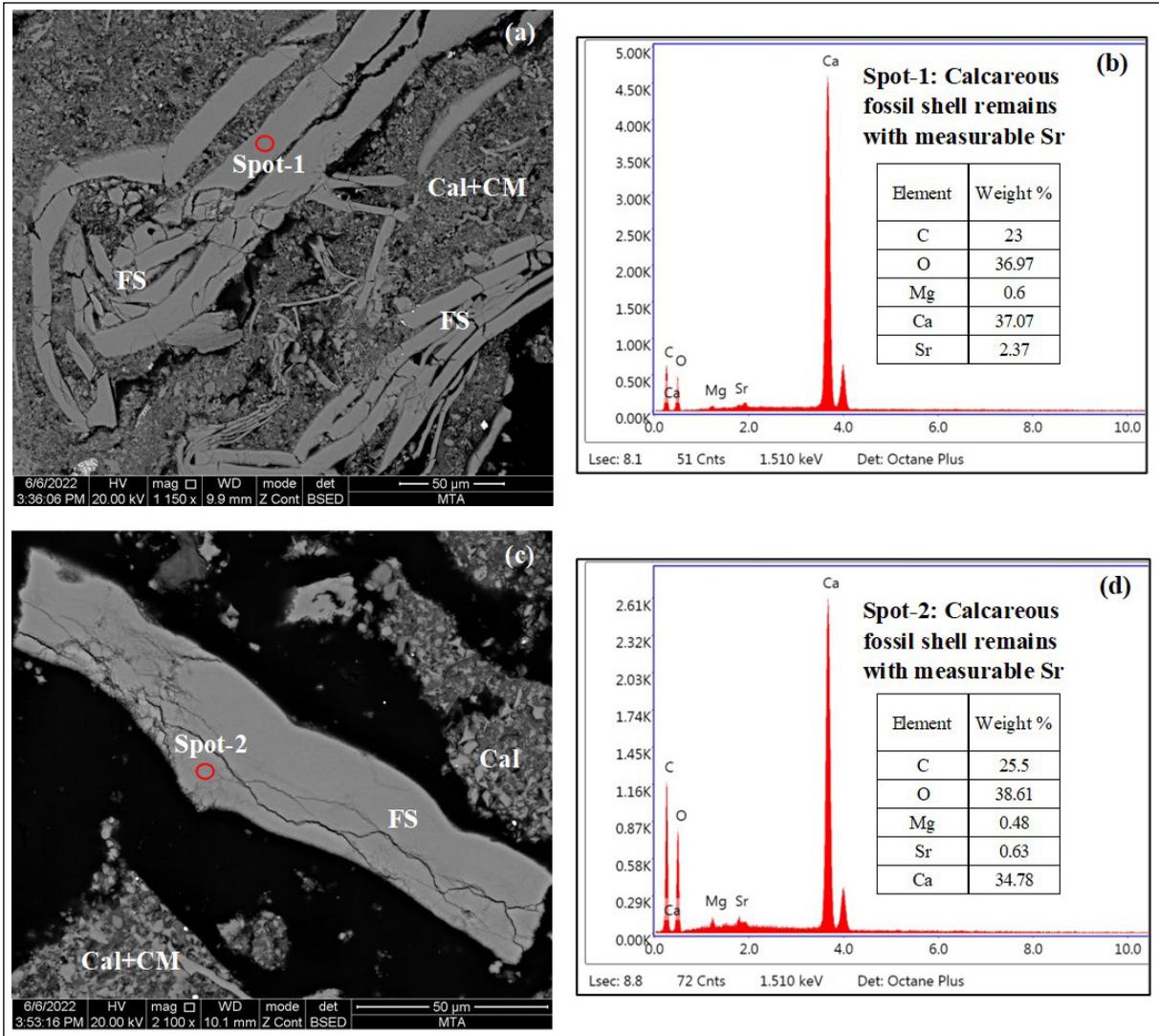
Figure 11- SEM-BSE images; a), c) SEM-EDX spectra of fossil shell (FS) in syngenetic carbonate (Cal), b) and d) SEM-EDX spectra of clay mineral (CM) matrix.

Table 7- Element affinities with ash yield (%, d) deduced from the calculation of Pearson's correlation coefficients.

Correlation with ash 0.70≤r<1.0
Al$_2$O$_3$, MgO, K$_2$O, Ga
Correlation with ash 0.40≤r<0.70
SiO$_2$, TiO$_2$, MnO, Sc, Cr, Rb, La, Ce, Eu, Gd, Tb
Correlation with ash r≥ -0.40
B, V, Mo, U, total S
Correlation with Al$_2$O$_3$ 0.70≤r<1.0
SiO$_2$, TiO$_2$, MgO, K$_2$O, Sc, Cr, Co, Ni, Zn, Ga, Rb, Y, La, Ce, Pr, Nd, Eu, Gd, Tb, Dy, Ho, Er, Yb, Th
Correlation with Al$_2$O$_3$ 0.40≤r<0.70
Na$_2$O, Li, Cu, Pb
Correlation with Fe$_2$O$_3$ 0.50≤r<1.0
Li, Ga, Co, Cu, Ni, Pb, Zn, total S
Correlation with CaO 0.50≤r<1.0
Ba, Sr
Correlation with total S 0.50≤r<1.0
B, Mo, V, As

The CaO displays a weak positive correlation with ash yields. The organic matter contains measurable by SEM-EDX amounts of Ca and S. This data implies an organic affinity for CaO. In Turkish Neogene coals, sulphate minerals, particularly gypsum/anhydrite, are reported as minor phases due to the evaporation of porewater during storage or reactions between liberated sulphuric acid from pyrite oxidation and CaO in porewater or organic matter (Karayiğit et al., 2017a, 2021). In contrast, gypsum/anhydrite are lacking from XRD and are also not identify during SEM examination. Although additional high-resolution analysis should be needed, measurable Ca and S in the organic matter might be an indicator for sub-micron sized gypsum/anhydrite grains (Finkelman et al., 2019; Dai et al., 2020b). Therefore, Ca seems having an inorganic rather than organic affinity. Supporting this assumption, the CaO concentrations are generally high in fossil shell fragments and syngenetic carbonate-bearing samples. Thus, the CaO in samples has a carbonate affinity. Furthermore, the CaO displays moderate positive correlations with Ba ($r_{CaO} = 0.67$) and Sr ($r_{CaO} = 0.65$). These correlations again imply the sulphate affinity for CaO, which is supported by measurable Ca from barite and celestine by SEM-EDX (Figures 12-14). Although CaO does not show any meaningful correlations with Al_2O_3 and P_2O_5, CaO in the samples could also be partially affiliated with apatite, Ca-phosphate fossil bone remains, and feldspar grains in the samples. Hence, CaO is mainly derived from carbonate minerals, and in a lower degree with sulphates, apatite and feldspars.

The Sr-enrichment in coal is related to epigenetic sulphate (e.g., celestine and Sr-bearing barite and gypsum/anhydrite) minerals, carbonate minerals (e.g., strontianite); and/or clastic feldspar grains, biogenic aragonite, and syngenetic phosphate and zeolite minerals (Pollock et al., 2000; Dai et al., 2012b, 2021; Karayiğit et al., 2020b; Spiro et al., 2019; Çelik et al., 2021; Du et al., 2021). In the studied samples, Sr, as mentioned above, only displays a positive moderate correlation with CaO. This correlation and the presence of measurable Sr in fossil shell remains could easily imply a carbonate affinity for Sr (Figure 11). However, this could be only applicable for some samples due to the presence of celestine and

Sr-bearing Cl/F-apatite grains in coal and roof rock samples (Figure 10a). In the roof rock sample, Sr is also measured from barite grains (Figures 13 and 14). Therefore, significantly high Sr concentrations in samples are mainly controlled by sulphate minerals. Furthermore, measurable Sr is not traced by SEM-EDX from organic matter, which indicating a clear inorganic affinity for Sr.

The B concentrations of the Bozburun coal samples are generally higher than 110 ppm (Table 4). Such concentrations could be evidence of paralic conditions (Goodarzi and Swaine, 1994; Goodarzi et al., 2020). The reported palynoflora and mollusc fauna from the Bozburun Formation suggest that freshwater conditions have been common (Türkmen et al., 2004; Nazik et al., 2008). The B-enrichment in coal was not always controlled by seawater and the presence of clay minerals or certain detritus accessory minerals (e.g., tourmaline). Boron uptake by peat-forming plants could cause B-enrichment (Boyd, 2002; Karayiğit et al., 2020a, b, 2021; Dai et al., 2021). The Turkish Neogene coals have B concentrations higher than 110 ppm despite their formation under freshwater conditions (Karayiğit et al., 2000; Tuncalı et al., 2002; Palmer et al., 2004). Boron have been derived from the wash-out from the volcanic rocks in the adjacent areas. Since middle Miocene volcanic rocks are close to the Bozburun coalfield, similar controlling parameters seem to have been developed for B enrichment. The strong negative correlation between B and ash yield (r_{ash} =-0.933) could easily indicate an organic affinity for B and possible B uptake by plants in the mires. Boron, however, could easily incorparted into clay minerals in the palaeomires, and the presence of clay minerals and illite/mica grains could also imply that B enrichment in the samples is also partially controlled by aluminosilicate minerals.

Chromium enrichment in Turkish Neogene coals is mostly related to clastic chromite grains derived from ophiolites in the basement (Karayiğit et al., 2000, 2020a, 2021; Palmer et al., 2004; Çelik et al., 2021). Ophiolites, like in other Turkish Neogene coalfields, are found in the Bozburun coalfield's adjacent areas (Figure 1a), and chromitites reported from these ophiolites (Uysal et al., 2007). However,
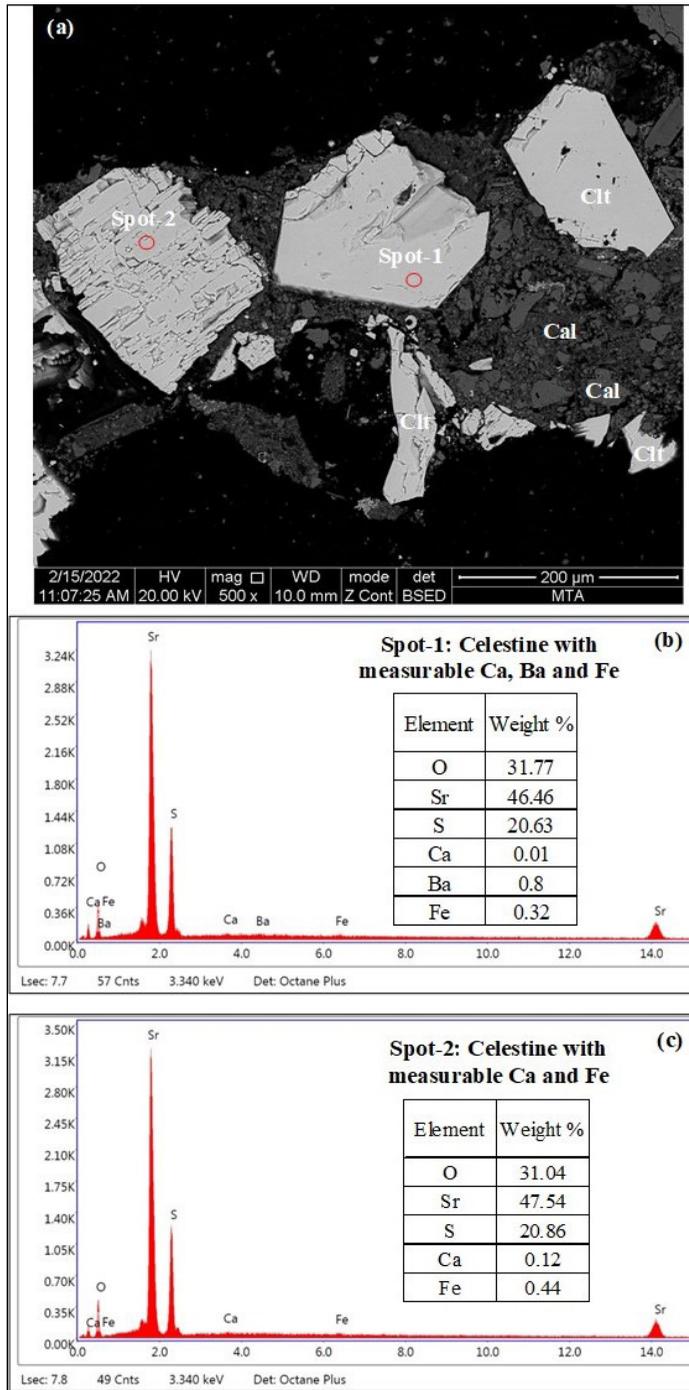
Figure 12-SEM-BSE images; a) SEM-EDX spectra, b), c) of authigenic celestine (Clt) grains within syngenetic carbonate (Cal) band.

chromite grains were not found in the samples during the SEM observations. Apart from clastic chromite grains, clastic input from ophiolitic rock within the palaeomire and their alteration by-products could control Cr enrichment of coal (Ruppert et al., 1996; Dai et al., 2021). In such cases, chlorite (chamosite) may contain Cr^{3+} and/or Fe^{3+} which could be partially replaced by Cr^{3+}. Considering the presence of clastic chlorite (chamosite) in the samples and strong positive correlations among Cr, Al_2O_3 SiO_2 and MgO (Table 7), it is possible that Cr enrichment was controlled by clastic chlorite grains. Nickel is another element

Element	Weight %
O	23.76
Sr	7.74
S	15.99
Ca	0.44
Ba	51.72
Fe	0.35

Spot 1: Sr-bearing barite (b)

Element	Weight %
O	28.35
Sr	20.74
S	17.88
Ba	33.02

Spot 2: Barite-celestine (c)

Element	Weight %
O	31.1
Sr	43.17
S	20.26
Ca	0.13
Ba	4.95
Fe	0.39

Spot 3: Celestine (d)
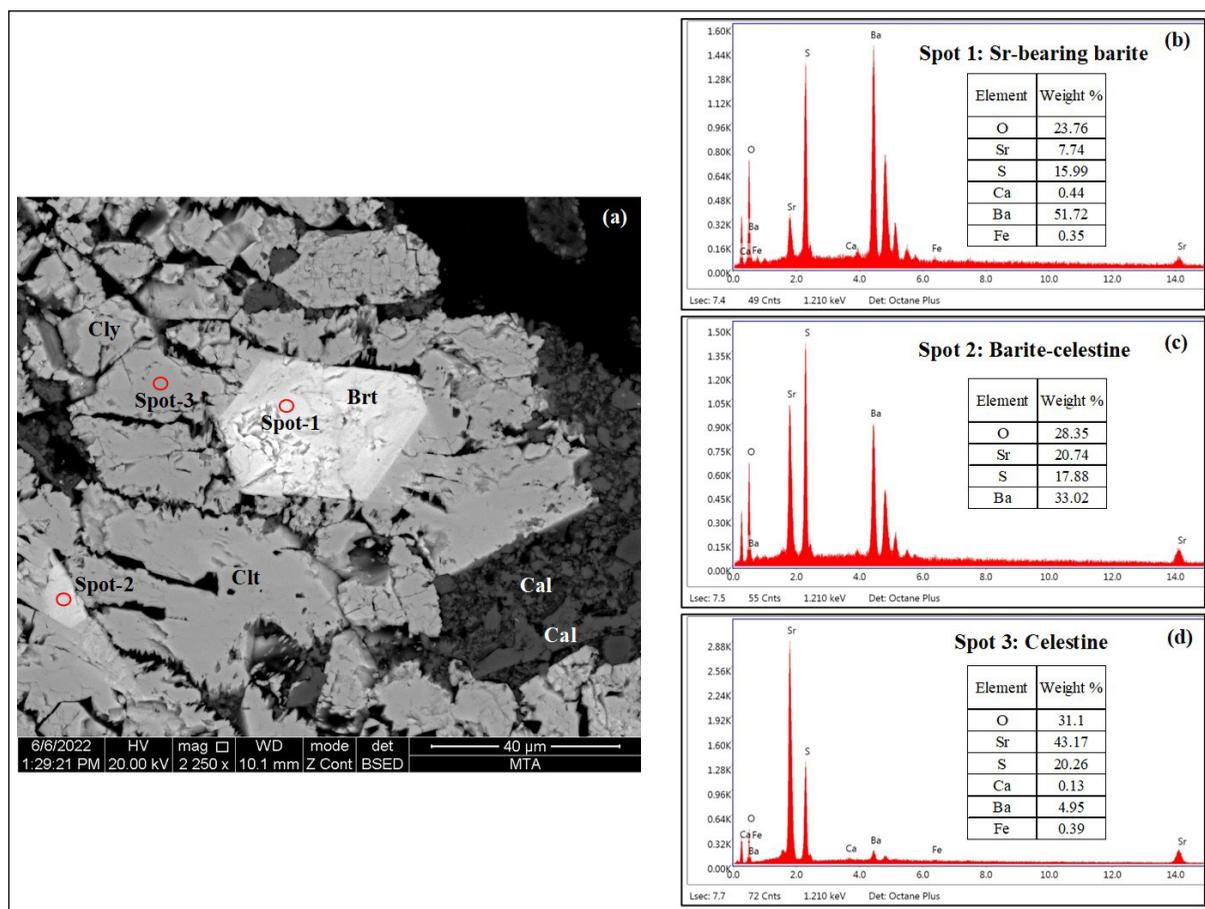
Figure 13- SEM-BSE images; a) SEM-EDX spectra, b), d) of barite (Brt) and celestine (Clt) within syngenetic carbonate (Cal) band.

which could be associated with clay minerals in coal or clastic input from the basement ophiolites (Ruppert et al., 1996). The positive moderate correlations among Ni, Al_2O_3, and SiO_2 also suggest an aluminosilicate affinity for Ni (Table 7); however, the SEM-EDX indicates another affinity for Ni. During the SEM-EDX studies, measurable Ni and As contents were detected in matrices of framboidal pyrite aggregates and/or marcasite overgrowths around nuclei of framboidal pyrite (Figure 15). As the samples contain more Ni- and As-bearing marcasite overgrowths, Ni and As enrichments in the coal samples might be took place during the late diagenetic stages The MnO does not display any significant correlation with ash yield, total S, or any other elements, which implies an intermediate affinity for MnO. In contrast, Mn is detected from euhedral framboidal grains (Figure 16). Hence, MnO shows a sulphide affinity. While elements Cu, Zn, and Pb were not detected in the framboidal pyrite grains, these elements generally display concentrations in

framboidal pyrite grains below the detection limit of conventional SEM equipment (Hower et al., 2008; Kolker, 2012). The moderate positive correlation between Fe_2O_3 and Zn can also be controlled by sphalerite grains in the samples (Figure 8b).

The elements V, Mo, and U also have negative correlations with ash yields (Table 7), which implies an organic affinity. Furthermore, V, Mo, and U elements show positive correlations with total S contents (Table 7), which are typical for Turkish Neogene coals. The enrichment of these elements in coal, on the other hand, could have been controlled by redox conditions (Arbuzov et al., 2011; Dai et al., 2021). These elements are generally enriched due to the development of anoxic conditions within the palaeomire and, in some cases, neutral to weak alkaline conditions. The latter one could be possible since fossil shell fragments and syngenetic carbonate bands are common in the samples. In the Turkish Neogene coals (e.g., Soma,
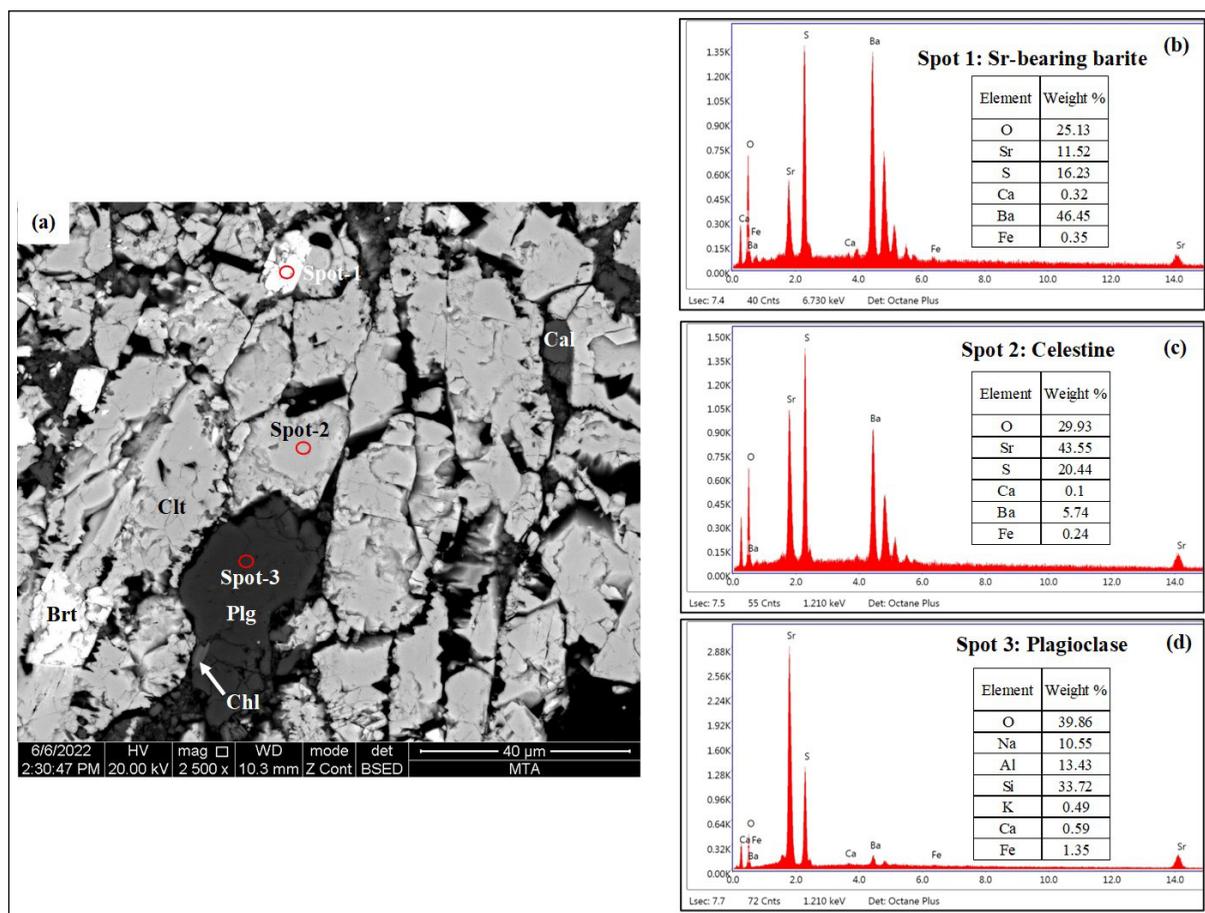
Figure 14- SEM-BSE images; a) and SEM-EDX spectra, b), d) of barite (Brt) and celestine (Clt) around clastic plagioclase (Plg) grain, and calcite (Cal) and chlorite (Chl).

Orhaneli, and Çayırhan coalfields), the alterations of synchronous volcanic input and/or clastic influx into the palaeomire could cause V, Mo, and U enrichment due to anoxic conditions (Querol et al., 1997; Palmer et al., 2004; Karayiğit et al., 2017a, 2021b, 2022). Considering that the middle Miocene volcanic rocks are exposed in the eastern margins of the coalfield, the source of V, Mo, and U could have been related to clastic input. These elements could be taken by peat-forming plants, like B; thus, they are enriched in coal samples. This could also explain their positive correlation with B.

5.4. Depositional Environment

The coal facies diagrams are the most common approach for assessing the depositional conditions during peat accumulation; nevertheless, these diagrams should be supported by sedimentological, palaeontological, mineralogical, and geochemical (e.g., biomarker) data from coal seams due to the complex nature of the peatlands and uncertainties about the origin of some macerals (Crosdale, 1993; Moore and Shearer, 2003; Oikonomopoulos et al., 2015; Dai et al., 2020a; Guo et al., 2020; Liu et al., 2020; Hower and Eble, 2022). Therefore, in this study, the coal facies data is interpreted along with elemental and mineralogical compositions of the studied samples, and published sedimentological, palaeontological, and organic-geochemical data from the Bozburun coalfield (Türkmen et al., 2004; Nazik et al., 2008; Yalçın-Erik and Ay, 2021). The coal samples are generally plotted close to the mid-point between the A and B apexes on Mukhopadhyay's (1989) ternary diagram (Figure 17). The presence of both woody and herbaceous peat-forming plants in the palaeomires resulted in such distribution. In addition, some mineral-rich samples from the low part of the seam are plotted close to apex B, which suggests the predominance of herbaceous
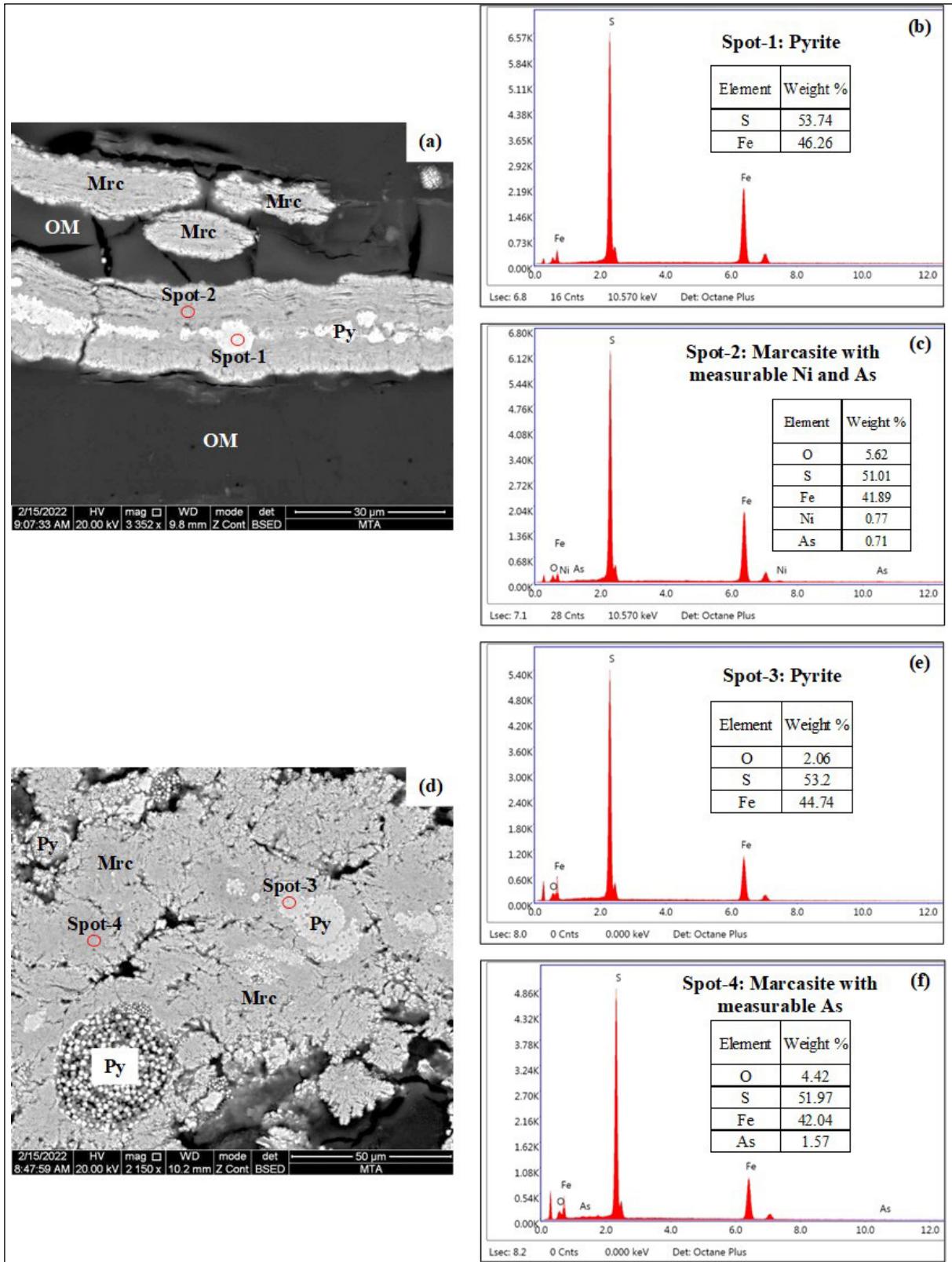
Figure 15- a), d) SEM-BSE images of pyrite (Py) and b), c), e) and f) SEM-EDX spectra (b, c, e and f) marcasite (Mrc).
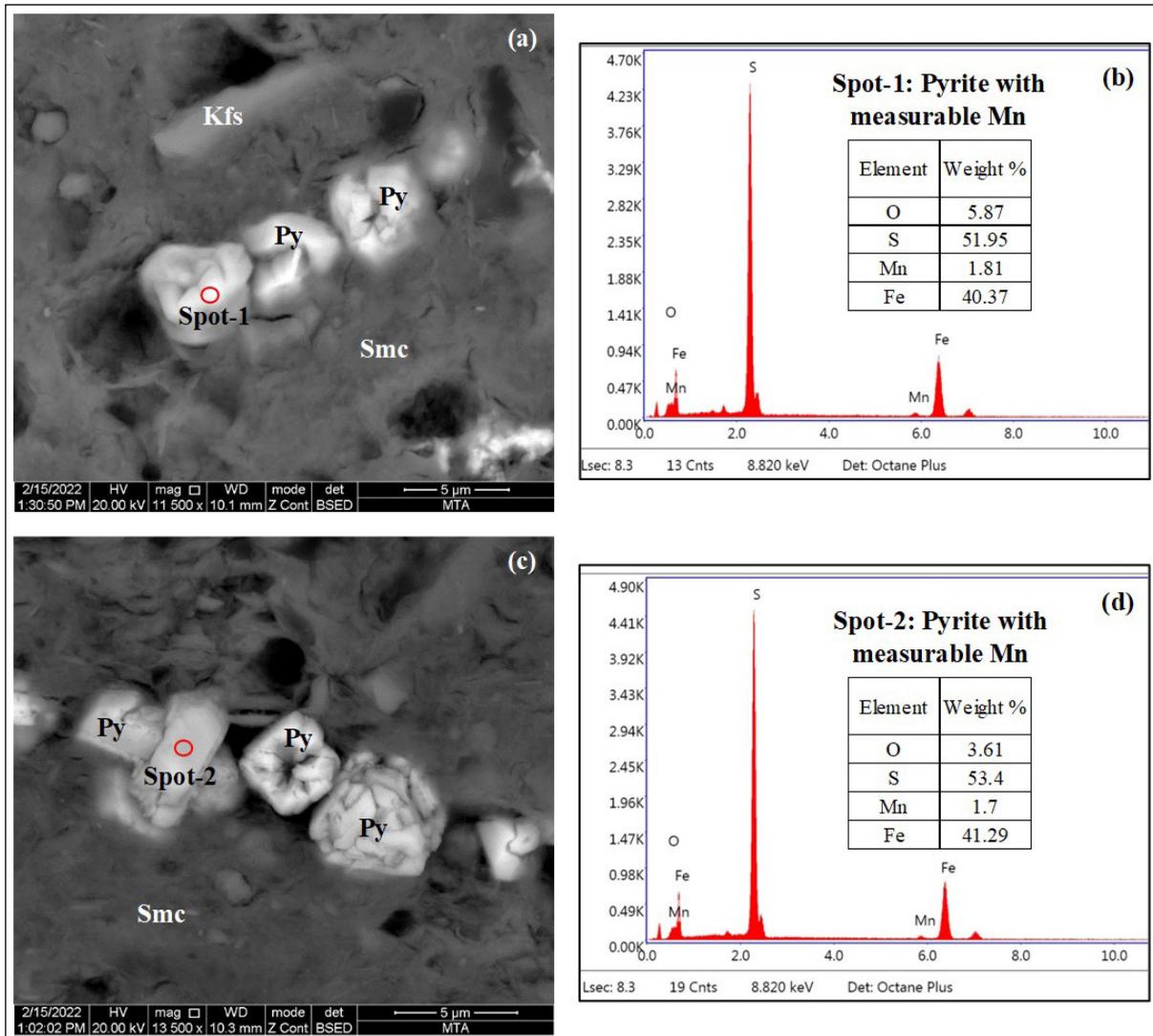
Figure 16- SEM-BSE images (a-c) and SEM-EDX spectra (b-d) of pyrite (Py) grains within smectite (Smc).

peat-forming plants and/or macrophyte in palaeomires. The relatively high total inertinite contents (> 10% on a mineral matter-free basis) of these samples could have been controlled by oxic conditions such as these caused by exposure of peat surface due to very low watertable and/or wildfires on palaeomire's surface or in the surrounding area (Figure 17). The presence of semifusinite and fusinite macerals in these coal samples are an indicator of wildfires within the palaeomire (O'Keefe et al., 2013; Hower et al., 2021). Char-rich lithotype should be observed in the studied coal seam a, if such thermal oxidation took place in the palaeomire (O'Keefe et al., 2013). In the studied profile, however, neither char-rich lithotypes nor char bands were observed. High inertinite contents do not always relate to oxic conditions in the palaeomire, and the presence of allochthonous inertinite macerals could result in higher inertinite contents (O'Keefe et al., 2013; Oskay et al., 2019). In the coal samples, semifusinite, fusinite, and inertodetrinite macerals are mostly associated with clay mineral aggregates and/or detrohuminite macerals. Thus, the high inertinite content in the low part of the seam are due to inertinite transport by surface water/windblown or mechanical degradation and subsequent oxidation in the palaeomire.

The Gelification Index (GI) *vs* Tissue Preservation Index (TPI) and the Groundwater Index (GWI) vs Vegetation (VI) diagrams were used in order to
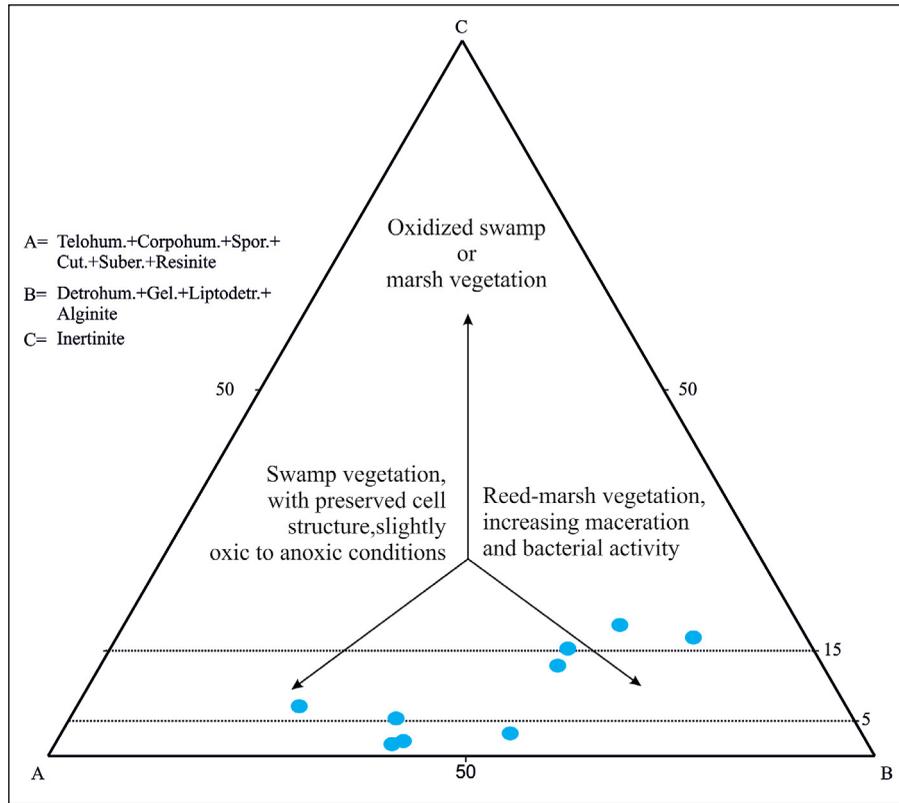
Figure 17- The Bozburun coal samples on Mukhopadhyay's ternary diagram (after Mukhopadhyay, 1989).

evaluate the preservation of organic matter and the vegetation type in the palaeomire (Figure 18). These diagrams were firstly proposed for late Palaeozoic coals of Canada and Australia by Calder et al. (1991) and Diessel (1992), respectively. Since the Cenozoic flora differs from the late Palaeozoic one, in this study the modifications proposed by Kalaitzidis et al. (2004) are applied. The TPI and VI values vary widely in the studied profile (Figure 18), which could imply variable preservation degree of organic matter and/or variations in the peat-forming vegetation. Additionally, the reported TPI (0.17-0.33) and VI (0.38-0.81) values from the western part of the Bozburun coalfield indicate vegetation variations in the palaeomire during the late Miocene (Yalçın-Erik and Ay, 2021). It is worth mentioning that the reported gelohuminite contents are very high in the western part of the Bozburun coalfield, which in turn, reduces TPI and VI values. Despite this, increasing trends of TPI and VI values towards the upper part of the studied profile were calculated (Figure 18 and Table 2). The TPI and VI values from the low part of the seam are generally lower than 1.0, which indicates the predominance

of herbaceous peat-forming plants during the initial stages of peat accumulation (Oskay et al., 2016; Guo et al., 2020). The presence of palynomorphs related to reed and macrophyte plants, as well as the short-chain *n*-alkanes in the Bozburun coalfield also support this assumption (Türkmen et al., 2004; Yalçın-Erik and Ay, 2021). Furthermore, freshwater gastropod remains and syngenetic carbonate bands in coal seam could also be another evidence for lakeshore (limno-telmatic) conditions and/or Ca-rich water influx into the palaeomire (Siavalas et al., 2009; Karayiğit et al., 2017a). Hence, the Ca concentration of the coal samples is significantly higher in this part of the seam (Figure 7 and Table 4), and alkaline conditions seem to be more common. Gelification of organic matter is supposed to be high due to bacterial activity forced by the increased alkalinity (Dehmer, 1995; Zdravkov et al., 2006; Stock et al., 2016); however, the GI values are generally lower than 1.0 in this part of the seam. Fluctuating water tables might also cause mechanical degradation of herbaceous plant matter and allochthonous inertinite macerals (Mach et al., 2013; O'Keefe et al., 2013). Thus, the attrinite and
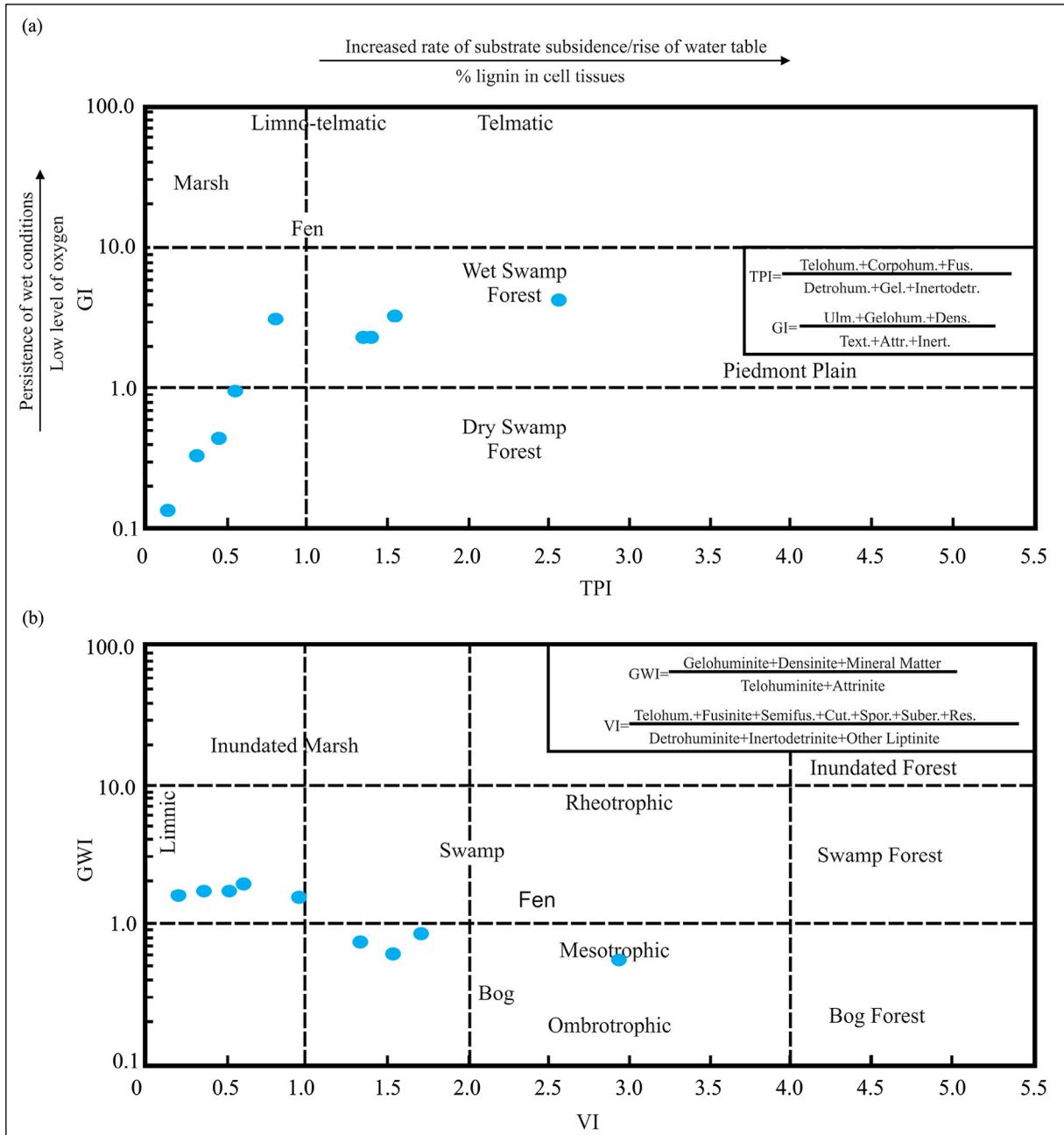
Figure 18- The distributions of the Bozburun coal samples on; a) GI vs. TPI plot of (after Diessel, 1992, modified from Kalaitzidis et al., 2004), b) VI vs. GWI plot of (after Calder et al., 1991, modified from Kalaitzidis et al., 2004).

inertodetrinite contents could be high; in turn, the GI values of the low part are low.

In contrast to the low profile part, the relatively higher TPI and VI values (Figure 18 and Table 2) in the central and upper parts of the seam imply an increased contribution of forested vegetation (Oikonomopoulos et al., 2015; Omodeo-Salé et al., 2017; Oskay et al., 2019; Karayiğit et al., 2020a). Furthermore, the reported existence of certain palynomorphs (e.g., *Inaperturopollenitis dubius*) and the long-chain *n*-alkanes point to coniferous peat-forming plants (Türkmen et al., 2004; Yalçın-Erik and Ay, 2021). This could also explain fluorescent ulminite A macerals in this part of seam, which is related to the presence of H-rich compounds in peat-forming plants and/or a coniferous peat-forming vegetation in the palaeomires

(Mastalerz et al., 2013; Karayiğit et al., 2017*b*, 2020*b*; Oskay et al., 2019; Kus et al., 2020). Such vegetation is typical for wet-forest mires in flood and/ or upper delta plains (Buillit et al., 2002). Supporting this assumption, previous sedimentological studies from the southern part of the Malatya Basin show that the Bozburun Formation was deposited under shallow lake and deltaic conditions. Furthermore, the watertable was generally stable and clastic influx could be low under such conditions; thus, anoxic conditions resulted in relatively good preservation of organic matter (Zdravkov et al., 2006; Mach et al., 2013; Kus et al., 2020). The anoxic conditions could be evident from the syngenetic framboidal pyrite grains and the decrease trend of ash yield upwards. The reported pristane/phytane (Pr/Rh) ratio from the Bozburun coalfield could also imply anoxic conditions (Yalçın-Erik and Ay, 2021). The GWI values of the coal samples from the upper part of the seam, however, are relatively low (Figure 18b), which is acceptable for telohuminite-rich coals (Kalaitzidis et al., 2004; Oikonomopoulos et al., 2015; Karayiğit et al., 2017*a*). The relatively high GI values and the syngenetic carbonate along with calcareous fossil remains could also imply that Ca-rich water influx and/or aquifer support into the palaeomire was continuous and gelification of organic matter is relatively high during the late stages of peat accumulation (Dehmer, 1995; Stock et al., 2016). Hence, the pH value of the mire water is alkaline, and concentrations of redox sensitive elements (e.g., Mo) are enriched in the upper part of the seam (Figure 7). The source of Ca-rich water could derive from the Palaeocene to late Eocene marine carbonates in the basement. As mentioned previously, these carbonates also contain gypsum layers; thus, the aquifer from these carbonates could also enrich the peat with sulphates. This supply could also cause the formation of authigenic sulphate minerals (e.g., celestine) since Sr is soluble in sulphate-rich waters (Honar, 2004). In general, the Sr/Ba ratios higher than 1 along with high total S content could be an indicator of marine influence during peat accumulation and/ or penetrating solutions from the overlying marine sediments (Spiro et al., 2019; Medunić et al., 2020; Lui et al., 2021). Both cases seem to have been impossible for the Bozburun coalfield, since only terrestrial and lacustrine conditions were developed in the

Malatya Basin during the late Miocene. As mentioned previously, the alteration of clastic feldspar grains from the middle Miocene volcanic rocks could be also provided additional Sr^{2+} ions. In turn, Sr/Ba ratios and total S contents of coal samples are elevated and could be high like paralic coals. Nevertheless, sulphate-rich water influx into the palaeomire may also cause weak brackish conditions, and this could explain the presence of freshwater to oligohaline mollusc fauna in the Bozburun coalfield and the presence of salinity indicator biomarkers (Nazik et al., 2008; Yalçın-Erik and Ay, 2021). Besides, the significantly high Ba and Sr contents could also indicate subsidence ratio during the late Miocene in the study area was optimal for the fixation of Ba and Sr in sulphate minerals in the palaoemires (Hower and Eble, 2022). Moreover, the varatitions on clastic-influx ratio, common peat-forming vegetation and mire water chemistry between western and eastern parts of the Bozburun coalfield seem to cause differences on coal quality parameters and mineralogy.

6. Results

Changes in peat-forming environment, redox conditions, clastic influx, and chemistry of water supply in the palaeomire have implications for coal quality, mineralogical, and elemental composition of the late Miocene coal seam in the eastern part of the Bozburun coalfield. The low part of the seam was accumulated under limnotelmatic conditions, which were open to clastic influx and water table fluctuation, and Ca-rich water influx was high into the palaeomire. Hence, detrohuminite, allochthonous inertinite, and calcareous fossil shell remains were commonly identified, and ash yields and volatile matter contents are relatively higher in this part of the seam. Furthermore, Ca-rich water influx resulted in the formation of neutral to weak alkaline conditions, which allowed authigenic formation of syngenetic carbonate minerals. Thus, CaO concentrations of the coal samples are significantly high in this part of the seam. The increasing trends of telohuminite proportions, TPI, and VI values towards the upper part of the seam could imply the formation of pure telmatic (wet-forest mire) conditions during the late stages of peat accumulation. Low clastic influx and stable water table conditions led to the establishment of anoxic conditions, in which authigenic framboidal

pyrite grains and marcasite overgrowth formed. Thus, chalcophile elements were enriched in the coal. Furthermore, continuous Ca-rich water influx into the palaeomire seems to control gelification of organic matter. The co-existence of syngenetic framboidal pyrite grains and carbonate minerals in the palaeomire of the upper part also implies weak acidic to neutral conditions; in turn, V, Mo and U are enriched in this part.

The high Sr/Ba ratios, the high total S contents and the presence of authigenic marcasite in the coal samples might be an indication of marine influence and/or penetration of porewater from overlying marine sediments. All these are clearly inapplicable in the Bozburun coalfield due to the freshwater mollusc remains, and the freshwater peat-forming plants according to previously published palaeontological and biomarker data. The formation of celestine and Ca- and Sr-bearing barite during diagenetic stages could be related to Sr-bearing sulphate-rich water influx into the palaeomire from gypsum-bearing Palaeogene and late Eocene carbonates and clastic feldspar grains from middle Miocene volcanic rocks. In addition, Sr uptake by mollusc fauna within the palaeomire could also cause elevated Sr-concentrations in fossil shell fragments-bearing coal and non-coal samples. Overall, the chemical composition of the water supplied the palaeomire and the redox conditions controlled the mineralogical and the elemental compositions in the eastern part of the Bozburun coalfield.

Acknowledgements

References

American Society for Testing and Materials (ASTM) D2797/D2797M. 2019. Standard practice for preparing coal samples for microscopical analysis by reflected light. ASTM International, 5.

American Society for Testing and Materials (ASTM) D388-19a. 2021. Standard classification of coals by rank. ASTM International, 8.

Arbuzov, S. I., Volostnov, A. V., Rikhvanov, L. P., Mezhibor, A. M., Ilenok, S. S. 2011. Geochemistry of radioactive elements (U, Th) in coal and peat of northern Asia (Siberia, Russian Far East, Kazakhstan, and Mongolia). International Journal of Coal Geology 86, 318-328.

Baysal, M., Yürüm, A., Yıldız, B., Yürüm, Y. 2016. Structure of some western Anatolia coals investigated by FTIR, Raman, ^{13}C solid state NMR spectroscopy and X-ray diffraction. International Journal of Coal Geology 163, 166-176.

Bohor, B. F., Triplehorn, D. M. 1993. Tonsteins: Altered volcanic-ash layers in coal-bearing sequences. Geological Society of America Special Papers 285, 1-44.

Boyd, R. J. 2002. The partitioning behaviour of boron from tourmaline during ashing of coal. International Journal of Coal Geology 53, 43-54.

Böning, P., Bard, E. 2009. Millennial/centennial-scale thermocline ventilation changes in the Indian Ocean as reflected by aragonite preservation and geochemical variations in Arabian Sea sediments. Geochimica et Cosmochimica Acta 73, 6771-6788.

Brisset, E., Djamali, M., Bard, E., Borschneck, D., Gandouin, E., Garcia, M., Stevens, L., Tachikawa, K. 2017. Late Holocene hydrology of Lake Maharlou, southwest Iran, inferred from high-resolution sedimentological and geochemical analyses. Journal of Paleolimnology 61, 111-128.

Buillit, N., Lallier-Vergès, E., Pradier, B., Nicolas, G. 2002. Coal petrographic genetic units in deltaic-plain deposits of the Campanian Mesa Verde Group (New Mexico, USA). International Journal of Coal Geology 51, 93-110.

Büçkün, Z., Inaner, H., Oskay, R. G., Christanis, K. 2015. Palaeoenvironmental reconstruction of Hüsamlar coal seam, SW Turkey. Journal of Earth System Science 124, 729-746.

Calder, J. H., Gibling, M. R., Mukhopadhyay, P. K. 1991. Peat formation in a Westphalian B piedmont setting, Cumberland Basin, Nova Scotia: implications for the maceral-based interpretation of rheotrophic and raised paleomires. Bulletin de la Société Géologique de France 162, 283-298.

Chen, Y., Zou, C., Mastalerz, M., Hu, S., Gasaway, C., Tao, X. 2015. Applications of micro-Fourier transform

infrared spectroscopy (FTIR) in the geological sciences-a review. International Journal of Molecular Sciences 16, 30223-30250.

Crosdale, P. J. 1993. Coal maceral ratios as indicators of environment of deposition: do they work for ombrogenous mires? An example from the Miocene of New Zealand. Organic Geochemistry 20, 797-809.

Çelik, Y., Karayiğit, A. I., Oskay, R. G., Kayseri-Özer, M. S., Christanis, K., Hower, J. C., Querol, X. 2021. A multidisciplinary study and palaeoenvironmental interpretation of middle Miocene Keles lignite (Harmancık Basin, NW Turkey), with emphasis on syngenetic zeolite formation. International Journal of Coal Geology 237, 103691.

Çetinkaya, S., Yürüm, Y. 2000. Oxidative pyrolysis of Turkish lignites in air up to 500°C. Fuel Processing Technology 67, 177-189.

Dai, S., Finkelman, R.B. 2018. Coal as a promising source of critical elements: Progress and future prospects. International Journal of Coal Geology 186, 155-164.

Dai, S., Ren, D., Chou, C-L., Finkelman, R. B., Seredin, V. V., Zhou, Y. 2012a. Geochemistry of trace elements in Chinese coals: A review of abundances, genetic types, impacts on human health, and industrial utilization. International Journal of Coal Geology 94, 3-21.

Dai, S., Zou, J., Jiang, Y., Ward, C., Wang, X., Li, T., Xue, W., Liu, S., Tian, H., Sun, X., Zhou, D. 2012b. Mineralogical and geochemical compositions of the Pennsylvanian coal in the Adaohai Mine, Daqingshan Coalfield, Inner Mongolia, China: Modes of occurrence and origin of diaspore, gorceixite, and ammonian illite. International Journal of Coal Geology 94, 250-270.

Dai, S., Liu, J., Ward, C. R., Hower, J. C., Xie, P., Jiang, Y., Hood, M. M., O'Keefe, J. M. K., Song, H. 2015a. Petrological, geochemical, and mineralogical compositions of the low-Ge coals from the Shengli Coalfield, China: A comparative study with Ge-rich coals and a formation model for coal-hosted Ge ore deposit. Ore Geology Reviews 71, 318-349.

Dai, S., Seredin, V. V., Ward, C. R., Hower, J. C., Xing, Y., Zhang, W., Song, W., Wang, P. 2015b. Enrichment of U–Se–Mo–Re–V in coals preserved within marine carbonate successions: geochemical and mineralogical data from the Late Permian Guiding Coalfield, Guizhou, China. Mineralium Deposita 50, 159-186.

Dai, S., Ward, C. R., Graham, I. T., French, D., Hower, J. C., Zhao, L., Wang, X. 2017. Altered volcanic ashes in coal and coal-bearing sequences: A review of their nature and significance. Earth-Science Reviews 175, 44-74.

Dai, S., Ji, D., Ward, C. R., French, D., Hower, J. C., Yan, X., Wei, Q. 2018. Mississippian anthracites in Guangxi Province, southern China: Petrological, mineralogical, and rare earth element evidence for high-temperature solutions. International Journal of Coal Geology 197, 84-114.

Dai, S., Bechtel, A, Eble, C. F., Flores, R. M., French, D., Graham, I. T., Hood, M. M., Hower, J. C., Korasidis, V. A., Moore, T. A., Püttmann, W., Wei, Q. 2020a. Recognition of peat depositional environments in coal: A review. International Journal of Coal Geology 219, 103383.

Dai S., Hower, J. C., Finkelman, R. B., Graham, I. T., French, D., Ward, C. R., Eskenazy, G., Wei, Q., Zhao, L. 2020b. Organic associations of non-mineral elements in coal: A review. International Journal of Coal Geology 218, 103347.

Dai S., Finkelman, R. B., French, D., Hower, J. C., Graham, I. T., Zhao, F. 2021. Modes of occurrence of elements in coal: A critical evaluation. Earth-Science Reviews 222, 103815.

Dehmer, J. 1995. Petrological and organic geochemical investigation of recent peats with known environments of deposition. International Journal of Coal Geology 28, 111-138.

Diessel, C. F. K. 1992. Coal-Bearing Depositional Systems. Springer, 721.

Di Giuseppe, P., Agostini, S., Di Vincenzo, G., Manetti, P., Savaşçın, M. Y., Conticelli, S. 2021. From subduction to strike slip-related volcanism: insights from Sr, Nd, and Pb isotopes and geochronology of lavas from Sivas–Malatya region, Central Eastern Anatolia. International Journal of Earth Sciences 110, 849-874.

Djowe, A. T., Laminsi, S., Njopwouo, D., Acayanka, E., Gaigneaux, E. M. 2013. Surface modification of smectite clay induced by non-thermal gliding arc plasma at atmospheric pressure. Plasma Chemistry and Plasma Processing 33, 707-723.

Du, F., Ning, S., Qiao, J., Tan, F., Zhao, X., Zhang, W., Li, C., Luo, Z., He, X. 2021. Geochemical and Mineralogical Characteristics of the Li-Sr-Enriched Coal in the Wenjiaba Mine, Guizhou, SW China. ACS Omega 6, 8816-8828.

Economic Commission for Europe-United Nations (E.C.E.-U.N.). 1998. International classification of in-seam coals. ECE, 41.

Ekici, T., Alpaslan, M., Parlak, O., Temel, A. 2007. Geochemistry of the Pliocene basalts erupted along the Malatya-Ovacik fault zone (MOFZ), eastern Anatolia, Turkey: Implications for source characteristics and partial melting processes. Geochemistry 67, 201-212.

Eminağaoğlu, M., Oskay, R. G., Karayiğit, A. I. 2022. Evaluation of elemental affinities in coal using agglomerative hierarchical clustering algorithm:

A case study in a thick and mineable coal seam (km²) from Soma Basin (W. Turkey). International Journal of Coal Geology 259, 104045.

Ercan, T., Asutay, H. J. 1993. Petrology of Neogene–Quaternary volcanics in Malatya-Elazığ-Tunceli-Bingöl-Diyarbakır region. Proceedings of A. Suat Erk Geology Symposium 2-5 September 1991, Ankara, 291–302 (in Turkish with English abstract).

Finch, A. A., Allison, N. 2008. Coordination of Sr and Mg in calcite and aragonite. Mineralogical Magazine 71, 539-552.

Finkelman, R. B., Dai, S., French, D. 2019. The importance of minerals in coal as the hosts of chemical elements. International Journal of Coal Geology 212, 103251.

Georgakopoulos, A., Iordanidis, A., Kapina, V. 2003. Study of low rank Greek coals using FTIR spectroscopy. Energy Sources 25, 995-1005.

Goodarzi, F., Swaine, D. J. 1994. The influence of geological factors on the concentration of boron in Australian and Canadian coals. Chemical Geology 118, 301-318.

Goodarzi, F., Gentzis, T., Hofmeister, H. 2020. Elemental composition of fluvial-lacustrine and lacustrine coal-bearing environments, British Columbia, Canada. Energy and Fuels 34, 16046-16058.

Guo, Q., Littke, R., Sun, Y., Zieger, L. 2020. Depositional history of low-mature coals from the Puyang Basin, Yunnan Province, China. International Journal of Coal Geology 221, 103428.

Hazra, B., Karacan, C. Ö., Tiwari, D. M., Singh, P. K., Singh, A. K. 2019. Insights from Rock-Eval analysis on the influence of sample weight on hydrocarbon generation from Lower Permian organic matter rich rocks, West Bokaro basin, India. Marine and Petroleum Geology 106, 160-170.

Honar, J. S. 2004. A model for the origin of large carbonate- and evaporite-hosted celestine ($SrSO_4$) deposits. Sedimentary Research 74, 168-175.

Hood, M. M., Eble, C. F., Hower, J. C., Dai, S. 2020. Geochemistry, petrology, and palynology of the Princess No. 3 coal, Greenup County, Kentucky. International Journal of Coal Science and Technology 7, 633-651.

Hower, J. C, Gayer, R. A. 2002. Mechanisms of coal metamorphism: case studies from Paleozoic coalfields. International Journal of Coal Geology 50, 215-245.

Hower, J. C., Eble, C. F. 2022. Petrology, palynology, and geochemistry of the Pond Creek coal (Pennsylvanian, Duckmantian), Pike County, Kentucky: Overprints of penecontemporaneous tectonism and peat doming. International Journal of Coal Geology 258, 104027.

Hower, J. C., Campbell, J. L. I., Teesdale, W. J., Nejedly, Z., Robertson, J. D. 2008. Scanning proton microprobe analysis of mercury and other trace elements in Fe-sulfides from a Kentucky coal. International Journal of Coal Geology 75, 88-92.

Hower, J. C, Eble, C. F., O'Keefe, J. M. K., Dai, S., Wang, P., Xie, P., Liu, J., Ward, C. R., French, D. 2015. Petrology, palynology, and geochemistry of Gray Hawk coal (Early Pennsylvanian, Langsettian) in Eastern Kentucky, USA. Minerals 5, 592-622.

Hower, J. C., Qian, D., Briot, N. J., Hood, M. M., Eble C. F. 2020. Mineralogy of a rare earth element-rich Manchester coal lithotype, Clay County, Kentucky. International Journal of Coal Geology 220, 103413.

Hower, J. C., Eble, C. F., O'Keefe, J. M. K. 2021. Phyteral perspectives: Every maceral tells a story. International Journal of Coal Geology 247, 103849.

Hower, J. C, Eble, C. F., Xie, P., Liu, J., Fu, B., Hood M. M. 2022. Aspects of rare earth element enrichment in Allegheny Plateau coals, Pennsylvania, USA. Applied Geochemistry 136, 105150.

International Committee for Coal Petrology (ICCP). 1993. International Handbook of Coal Petrography, Centre National de la Recherche Scientifique, 146.

International Committee for Coal Petrology (ICCP). 2001. New inertinite classification (ICCP System 1994). Fuel 80, 459-471.

International Standard Organisation (ISO) 11760. 2005. Classification of coals. International Organization for Standardization, 9.

Jarvie, D. M., Claxton, B. L., Henk, F., Breyer, J. T. 2001. Oil and shale gas from the Barnett Shale, Fort Worth basin, Texas. AAPG Annual Convention, Denver, Colorado, AAPG Search and Discovery Article.

Jiang, J., Zhang, S., Longhurst, P., Yang, W., Zheng, S. 2021. Molecular structure characterization of bituminous coal in Northern China via XRD, Raman and FTIR spectroscopy. Spectrochimica Acta - Part A: Molecular and Biomolecular Spectroscopy 255, 119724.

Kalaitzidis, S., Bouzinos, A., Papazisimou, S., Christanis, K. 2004. A short-term establishment of forest fen habitat during Pliocene lignite formation in the Ptolemais Basin, NW Macedonia, Greece. International Journal of Coal Geology 57, 243-263.

Karayiğit, A. İ., Whateley, M. K. G. 1997. The origin and properties of a coal seam associated with continental thin micritic limestones, Selimoglu-Divrigi, Turkey. Geological Society Special Publication 125, 101-114.

Karayiğit, A. İ., Gayer, R. A. 2000. Trace elements in a Pliocene-Pleistocene lignite profile from the Afsin-Elbistan field, Eastern Turkey. Energy Sources 22, 13-21.

Karayiğit, A. İ., Gayer, R. A., Querol, X., Onacak, T. 2000. Contents of major and trace elements in feed coals from Turkish coal-fired power plants. International Journal of Coal Geology 44, 69-184.

Karayiğit, A. İ., Gayer, R. A., Ortac, F. E., Goldsmith, S. 2001. Trace elements in the Lower Pliocene fossiliferous Kangal lignites, Sivas, Turkey. International Journal of Coal Geology 47, 73-89.

Karayiğit, A. İ., Oskay, R. G., Tuncer, A., A. Gümüş, B., Şengüler, İ., Yaradılmış, H., Tunoğlu, C. 2016. A multidisciplinary study of the Gölbaşı-Harmanlı coal seam, SE Turkey. International Journal of Coal Geology 167, 31-47.

Karayiğit, A. İ., Littke, R., Querol, X., Tim, J., Oskay, R. G., Kimon, C. 2017*a*. The Miocene coal seams in the Soma Basin (W. Turkey): Insights from coal petrography, mineralogy and geochemistry. International Journal of Coal Geology 173, 110-128.

Karayiğit, A. İ., Bircan, C., Mastalerz, M., Oskay, R. G., Querol, X., Lieberman, N. R., Türkmen, İ. 2017*b*. Coal characteristics, elemental composition and modes of occurrence of some elements in the İsaalan coal (Balıkesir, NW Turkey). International Journal of Coal Geology 172, 43-59.

Karayiğit, A. İ., Mastalerz, M., Oskay, R. G., Gayer, R. A. 2018. Coal petrography, mineralogy, elemental compositions and palaeoenvironmental interpretation of late Carboniferous coal seams in three wells from the Kozlu coalfield (Zonguldak Basin, NW Turkey). International Journal of Coal Geology 187, 54-70.

Karayiğit, A. İ., Oskay, R. G., Gayer, R. A. 2019. Mineralogy and geochemistry of feed coals and combustion residues of the Kangal power plant (Sivas, Turkey). Turkish Journal of Earth Sciences 28, 436-456.

Karayiğit, A. İ., Atalay, M., Oskay, R. G., Córdoba, P., Querol, X., Bulut, Y. 2020*a*. Variations in elemental and mineralogical compositions of Late Oligocene, Early and Middle Miocene coal seams in the Kale-Tavas Molasse sub-basin, SW Turkey. International Journal of Coal Geology 218, 103366.

Karayiğit, A. İ., Bircan, C., Oskay, R. G., Türkmen, İ., Querol, X. 2020*b*. The geology, mineralogy, petrography, and geochemistry of the Miocene Dursunbey coal within fluvio-lacustrine deposits, Balıkesir (Western Turkey). International Journal of Coal Geology 228, 103548.

Karayiğit, A. İ., Yerin, Ü. O., Oskay, R. G., Bulut, Y., Córdoba, P. 2021. Enrichment and distribution of elements in the middle Miocene coal seams in the Orhaneli coalfield (NW Turkey). International Journal of Coal Geology 247, 103854.

Kaymakçı, N., İnceöz, M., Ertepınar, P. 2006. 3D-architecture and neogene evolution of the Malatya basin: inferences for the kinematics of the Malatya and Ovacık Fault zones. Turkish Journal of Earth Sciences 15, 123-154.

Ketris, M. P., Yudovich Ya. E. 2009. Estimations of Clarkes for carbonaceous biolithes: World averages for trace element contents in black shales and coals. International Journal of Coal Geology 78, 135-148.

Kocaaslan, A., Ersoy, Y. E. 2018. Petrologic evolution of Miocene-Pliocene mafic volcanism in the Kangal and Gürün basins (Sivas-Malatya), central east Anatolia: Evidence for Miocene anorogenic magmas contaminated by continental crust. Lithos 310-311, 392-408.

Koç-Taşgın, C. 2011. Seismically-generated hydroplastic deformation structures in the Late Miocene lacustrine deposits of the Malatya Basin, eastern Turkey. Sedimentary Geology 235, 264-276.

Kolker, A. 2012. Minor element distribution in iron disulfides in coal: A geochemical review. International Journal of Coal Geology 94, 32-43.

Kortenski, J. 1992. Carbonate minerals in Bulgarian coals with different degrees of coalification. International Journal of Coal Geology 20, 225-242.

Kus, J., Dolezych, M., Schneider, W., Hofmann, T., Visiné-Rajczi, E. 2020. Coal petrological and xylotomical characterization of Miocene lignites and in-situ fossil tree stumps and trunks from Lusatia region, Germany: palaeoenvironment and taphonomy assessment. International Journal of Coal Geology 217, 103283.

Langston, W. J., Bebianno, M. J., Burt, G. R. 1998. Metal handling strategies in molluscs. Langston, W. J. and Bebianno, M. J. (Ed.). Metal metabolism in aquatic environments. Chapman and Hall. London, 219-283.

Liu, J., Dai, S., Hower, J. C., Moore, T. A., Moroeng, O., Nechaev, V. P., Petrenko, T. I., French, D., Graham, I. T., Song, X. 2020. Stable isotopes of organic carbon, palynology, and petrography of a thick low-rank Miocene coal within the Mile Basin, Yunnan Province, China: implications for palaeoclimate and sedimentary conditions. Organic Geochemistry 149, 104103.

Mach, K., Sýkorová, I., Konzalová, M., Opluštil, S. 2013. Effect of relative lake-level changes in mire-lake system on the petrographic and floristic compositions of a coal seam, in the Most Basin (Miocene), Czech Republic. International Journal of Coal Geology 105, 120-136.

Madejova, J. 2003. FTIR techniques in clay mineral studies. Vibrational Spectroscopy 31, 1-10.

Marcano, M. C., Frank, T. D., Mukasa, S. B., Lohmann, K. C., Taviani, M. 2015. Diagenetic incorporation of Sr into aragonitic bivalve shells: implications for chronostratigraphic and palaeoenvironmental interpretations. Depositional Record 1, 38-52

Mastalerz, M., Hower, J. C., Taulbee, D. N. 2013. Variations in chemistry of macerals as reflected by micro-scale analysis of a Spanish coal. Geologica Acta 11, 483-493.

Medunić, G., Grigore, M., Dai, S., Berti, D., Hochella, M. F., Mastalerz, M., Valentim, B., Guedes, A., Hower, J. C. 2020. Characterization of superhigh-organic-sulfur Raša coal, Istria, Croatia, and its environmental implication. International Journal of Coal Geology 217, 103344.

Moore, T. A., Shearer, J. C. 2003. Peat/coal type and depositional environment – are they related? International Journal of Coal Geology 56, 233-252.

Mukhopadhyay, P. 1989. Organic petrography and organic geochemistry of tertiary coals from texas in relation to depositional environment and hydrocarbon generation. Report of Investigations, Bureau of Economic Geology, 118.

Nadkarni, R. A. 1980. Multitechnique multielemental analysis of coal and fly ash. Analytical Chemistry 52, 929-935.

Naik, A. S., Behera, B., Shukla, U. K., Sahu, H. B., Singh, P. K., Mohanty, D., Sahoo, K., Chatterjee, D. 2021. Mineralogical Studies of Mahanadi Basin coals based on FTIR, XRD and Microscopy: A Geological Perspective. Journal of the Geological Society of India 97, 1019-1027.

Nazik, A., Türkmen, I., Koç, C., Aksoy, E., Avşar, N., Yayık, H. 2008. Fresh and brackish water ostracods of Upper Miocene deposits, Arguvan/Malatya (Eastern Anatolia). Turkish Journal of Earth Sciences 17, 481-495.

Oikonomopoulos I. K., Perraki, M., Tougiannidis, N., Perraki T., Frey M. J., Antoniadis, P., Ricken, W. 2013. A comparative study on structural differences of xylite and matrix lignite lithotypes by means of FT-IR, XRD, SEM and TGA analyses: An example from the Neogene Greek lignite deposits. International Journal of Coal Geology 115, 1-12.

Oikonomopoulos, I. K., Kaouras, G., Tougiannidis, N., Ricken, W., Gurk, M., Antoniadis, P. 2015. The depositional conditions and the palaeoenvironment of the Achlada xylite-dominated lignite in western Makedonia, Greece. Palaeogeography, Palaeoclimatology, Palaeoecology 440, 777-792.

O'Keefe, J. M. K., Bechtel, A., Christanis, K., Dai, S., DiMichele, W. A., Eble, C. F., Esterle, J. S., Mastalerz, M., Raymond, A. L., Valentim, B. V., Wagner, N. J., Ward, C. R. 2013. On the fundamental difference between coal rank and coal type. International Journal of Coal Geology 118, 58-87.

Omodeo-Salé, S., Deschamps, R., Michel, P., Chauveau, B., Suárez-Ruiz, I. 2017. The coal-bearing strata of the lower cretaceous Mannville Group (Western Canadian sedimentary basin, South Central Alberta), part 2: factors controlling the composition of organic matter accumulations. International Journal of Coal Geology 179, 219-241.

Oskay, R. G., Christanis, K., Inaner, H., Salman, M., Taka, M. 2016. Palaeoenvironmental reconstruction of the eastern part of the Karapınar-Ayrancı coal deposit (Central Turkey). International Journal of Coal Geology 163, 100-111.

Oskay, R. G., Bechtel, A., Karayiğit, A. İ. 2019. Mineralogy, petrography and organic geochemistry of Miocene coal seams in the Kınık coalfield (Soma Basin-Western Turkey): Insights into depositional environment and palaeovegetation. International Journal of Coal Geology 210, 103205.

Önal, M. 1995. Stratigraphy, coal potential and neotectonics of Malatya graben. Süleyman Demirel Üniversitesi, Mühendislik Mimarlık Fakültesi Jeoloji Seksiyonu 8, 159-175 (in Turkish with English abstract).

Palmer, C. A., Tuncali, E., Dennen, K. O., Coburn, T. C., Finkelman, R. B. 2004. Characterization of Turkish coals: a nationwide perspective. International Journal of Coal Geology 60, 85-115.

Pickel, W., Kus, J., Flores, D., Kalaitzidis, S., Christanis, K., Cardott, B. J., Misz-Kennan, M., Rodrigues, S., Hentschel, A., Hamor-Vido, M., Crosdale, P., Wagner, N., ICCP. 2017. Classification of liptinite-ICCP System 1994. International Journal of Coal Geology 169, 40-61.

Pollock, S. M., Goodarzi, F., Riediger, C. L. 2000. Mineralogical and elemental variation of coal from Alberta, Canada: an example from the No. 2 seam, Genesee Mine. International Journal of Coal Geology 43, 259-286.

Querol, X., Chinenon S., Lopez-Soler A. 1989. Iron sulfide precipitation sequence in Albian coals from the Maestrazgo Basin, southeastern Iberian Range, northeastern Spain. International Journal of Coal Geology 11, 171-189.

Querol, X., Whateley, M. K. G., Fernández-Turiel, J. L., Tuncalı, E. 1997. Geological controls on the mineralogy and geochemistry of the Beypazari lignite, central Anatolia, Turkey. International Journal of Coal Geology 33, 255-271.

Querol, X., Alastuey, A., Plana, F., Lopez-Soler, A., Tuncalı, E., Toprak, S., Ocakoğlu, F., Köker, A. 1999. Coal geology and coal quality of the Miocene Mugla basin, southwestern Anatolia, Turkey. International Journal of Coal Geology 41, 311-332.

Rieder, M., Crelling, J. C., Šustai, O., Drábek M., Weiss, Z., Klementová, M. 2007. Arsenic in iron disulfides in a brown coal from the North Bohemian Basin,

Czech Republic. International Journal of Coal Geology 71, 115-121.

Ruppert, L., Finkelman, R., Boti, E., Milosavljevic, M., Tewalt, S., Simon, N., Dulong, F. 1996. Origin and significance of high nickel and chromium concentrations in pliocene lignite of the Kosovo Basin, Serbia. International Journal of Coal Geology 29, 235-258.

Ruppert, L. F., Hower, J. C., Eble, C. F. 2005. Arsenic-bearing pyrite and marcasite in the Fire Clay coal bed, Middle Pennsylvanian Breathitt Formation, eastern Kentucky. International Journal of Coal Geology 63, 27-35.

Sançar, T., Zabcı, C., Karabacak, V., Yazıcı, M., Akyüz, H. S. 2019. Geometry and Paleoseismology of the Malatya Fault (Malatya-Ovacık Fault Zone), Eastern Turkey: Implications for intraplate deformation of the Anatolian Scholle. Journal of Seismology 23, 319-340.

Seredin, V. V., Dai, S. 2012. Coal deposits as potential alternative sources for lanthanides and yttrium. International Journal of Coal Geology 94, 67-93.

Seyitoğlu, G., Aktuğ, B., Esat, K., Kaypak, B. 2022. Neotectonics of Turkey (Türkiye) and surrounding regions: a new perspective with block modelling. Geologica Acta 20(4), 1-21.

Siavalas, G., Linou, M., Chatziapostolou, A., Kalaitzidis, S., Papaefthymiou, H., Christanis, K. 2009. Palaeoenvironment of seam I in the Marathousa lignite mine, Megalopolis basin (southern Greece). International Journal of Coal Geology 78, 233-248.

Sümengen, M. 2016. Malatya-K40 sheet. 1:100.000 scaled Series of Geological Maps of Turkey. General Directorate of Mineral Research and Exploration Publication, 29.

Spiro, B. F., Liu, J., Dai, S., Zeng, R., Large, D., French, D. 2019. Marine derived $^{87}Sr/^{86}Sr$ in coal, a new key to geochronology and palaeoenvironment: elucidation of the India-Eurasia and China-Indochina collisions in Yunnan, China. International Journal of Coal Geology 215, 103304.

Stock, A. T., Littke, R., Lücke, A., Zieger, L., Thielemann, T. 2016. Miocene depositional environment and climate in western Europe: The lignite deposits of the Lower Rhine Basin, Germany. International Journal of Coal Geology 157, 2-18.

Sütçü, E. C., Karayiğit, A. İ. 2015. Mineral matter, major and trace element content of the Afşin-Elbistan coals, Kahramanmaraş, Turkey. International Journal of Coal Geology 144-145, 111-129.

Swaine, D. J. 1990. Trace Elements in Coal. Butterworth, 278.

Sýkorová, I., Pickel, W., Christanis, K., Wolf, M., Taylor, G. H., Flores, D. 2005. Classification of huminite -

ICCP System 1994. International Journal of Coal Geology 62, 85-106.

Tekin, E., Varol, B., Ayan, Z., Satır, M. 2002. Epigenetic origin of celestite deposits in the Tertiary Sivas Basin: new mineralogical and geochemical evidence. Neues Jahrbuch für Mineralogie - Monatshefte 7, 289-318.

Tuncalı, E., Çiftçi, B., Yavuz, N., Toprak, S., Köker, A., Gencer, Z., Ayçık, H., Pahin, N. 2002. Chemical and technological properties of Turkish Tertiary coals. General Directorate of Mineral Research and Exploration Publication, 401.

Türkmen, İ., Aksoy, E., Koç, C. 2007. Alluvial and lacustrine facies in an extensional basin: Miocene of the Malatya Basin, eastern Turkey. Journal of Asian Earth Sciences 30, 181-198.

Türkmen, İ., Koç, C., Aksoy, E., Avşar, N., Dinçer, F. 2004. Stratgraphy and depositional environments of Neogene units in the area of Arguvan-Bozburun (Malatya, E. Turkey). Geosound/Yerbilimleri 44-45, 57-73 (in Turkish with English abstract).

Türkmen, İ., Taşgin, C. K., Avşar, N., Aksoy, E. 2011. Sedimentological characteristics of Alibonca Formation (Upper Oligocene-Lower Miocene) near Arapgir-Yoncalı area (Malatya). Yerbilimleri/ Earth Sciences 32, 235-254 (in Turkish with English abstract).

Uysal, I., Zaccarini, F., Garuti, G., Meisel, T., Tarkian, M., Bernhardt, H. J., Sadıklar, M. B. 2007. Ophiolitic chromitites from the Kahramanmaras area, southeastern Turkey: Their platinum-group elements (PGE) geochemistry, mineralogy and Os-isotope signature. Ofioliti 32, 151-161.

Ward, C. F. 2002. Analysis and significance of mineral matter in coal seams. International Journal of Coal Geology 50, 135-168.

Xu, N., Xu, C., Finkelman, R. B., Engle, M. A., Li, Q., Peng, M., He, L., Huang, B., Yang, Y. 2022. Coal elemental (compositional) data analysis with hierarchical clustering algorithms. International Journal of Coal Geology 249, 103892.

Yalçın-Erik, N., Ay, F. 2021. Use of petrological and organic geochemical data in determining hydrocarbon generation potential of coals: miocene coals of Malatya Basin (Eastern Anatolia-Turkey). International Journal of Coal Science and Technology 8, 510-533.

Yılmaz, Y. 2019. Southeast Anatolian Orogenic Belt revisited (geology and evolution). Canadian Journal of Earth Sciences 56, 1163-1180.

Zdravkov, A., Kostova, I., Sachsenhofer, R. F., Korstenski, J. 2006. Reconstruction of paleoenvironment during coal deposition in the Neogene Karlovo graben, Bulgaria. International Journal of Coal Geology 67, 79-94.